



Development of smart boulders to monitor mass movements via the Internet of Things: A pilot study in Nepal

Benedetta Dini¹, Georgina L. Bennett², Aldina M. A. Franco¹, Michael R. Z. Whitworth³, Kristen L. Cook⁴, Andreas Senn⁵, John M. Reynolds⁶

¹School of Environmental Sciences, University of East Anglia, Norwich Research Park, UK; ²College of Life and Environmental Sciences, University of Exeter, UK; ³AECOM, UK; ⁴GFZ-Potsdam, Germany; ⁵Miromico AG, Zurich, Switzerland; ⁶Reynolds International Ltd, UK

1 Abstract

2 Boulder movement can be observed not only in rock fall activity, but also in association with other
3 landslide types such as rock slides, soil slides in colluvium originated from previous rock slides and
4 debris flows. Large boulders pose a direct threat to life and key infrastructure, amplifying landslide
5 and flood hazards, as they move from the slopes to the river network. Despite the hazard they pose,
6 boulders have not been directly targeted as a mean to detect landslide movement or used in dedicated
7 early warning systems. We use an innovative monitoring system to observe boulder movement
8 occurring in different geomorphological settings, before reaching the river system. Our study focuses
9 on an area in the upper Bhote Koshi catchment northeast of Kathmandu, where the Araniko highway
10 is subjected to periodic landsliding and floods during the monsoons and was heavily affected by
11 coseismic landslides during the 2015 Gorkha earthquake. In the area, damage by boulders to
12 properties, roads and other key infrastructure, such as hydropower plants, is observed every year. We
13 embedded trackers in 23 boulders spread between a landslide body and two debris flow channels,
14 before the monsoon season of 2019. The trackers, equipped with accelerometers, can detect small
15 angular changes in boulders orientation and large forces acting on them. The data can be transmitted
16 in real time, via a long-range wide area network (LoRaWAN[®]) gateway to a server. Nine of the tagged
17 boulders registered patterns in the accelerometer data compatible with downslope movements. Of
18 these, six lying within the landslide body show small angular changes, indicating a reactivation during
19 the rainfall period and a movement consistent with the landslide mass. Three boulders, located in a
20 debris flow channel, show sharp changes in orientation, likely corresponding to larger free movements



21 and sudden rotations. This study highlights that this innovative, cost-effective technology can be used
22 to monitor boulders in hazard prone sites, identifying in real time the onset of movement, and may
23 thus set the basis for early warning systems, particularly in developing countries, where expensive
24 hazard mitigation strategies may be unfeasible.

25 1. Introduction

26 Landslides that affect and originate from mountainous bedrock hillslopes often contain boulders, large
27 fragments with diameter > 0.25 m and up to several metres. These boulders may have a significant
28 influence on the fluvial network in terms of landscape evolution, a topic receiving increased attention
29 in the recent literature (e.g. Shobe et al., 2020; Bennett et al., 2016). However, the presence in varying
30 proportions of large grain sizes within a landslide mass can also significantly influence its destructive
31 power and affect recovery operations. Large boulders can instantaneously destroy properties,
32 infrastructure and, critically, they can block lifelines for considerable periods of time, as they are the
33 most difficult component of a deposit to remove (e.g. Serna & Panzar, 2018). Boulders can lie on
34 hillslopes for a long time, before being remobilised as a consequence of trigger events, such as intense
35 rainfall and earthquakes, which may lead to hazard cascade chains involving boulder transport. In
36 time, boulders have the potential to move from hillslopes and to enter debris flow channels and
37 eventually rivers, posing a hazard along the way. Among the far-reaching effects of boulder
38 movements, damage to hydropower dams can have significant knock-on effects on local economies
39 (e.g. Reynolds, 2018a,b,c). Despite the potential that boulders have to amplify both landslide and
40 floods hazards and despite their ubiquitous occurrence, their presence, their movement and their
41 damaging power has neither been widely nor directly quantified in the available literature.

42 The direct and accurate monitoring of boulder movement, also in relation to environmental variables,
43 is essential in order to achieve a better understanding of the implications of their presence on
44 hillslopes in active landscapes, the dynamics of their remobilisation and their eventual entrainment in
45 river systems. In this context, boulder tracking and real-time monitoring represents an important step



46 forward towards increased resilience in hazard prone areas and it could be performed in different
47 geomorphological settings, ranging from landslide bodies, to loose slope deposits, to debris flow
48 channels and rivers, depending on the specific needs and aims. The ability to produce alerts for either
49 hazardous boulder movements, or to use the movement of boulders to identify hazardous
50 reactivations of existing large instabilities, requires the careful choice of monitoring techniques that
51 work in difficult and different environments, preferably wireless and that can reliably send information
52 in real time. Whilst various early warning systems have been experimented with and put in place for
53 landslides and debris flows, no early warning system has been used to detect and monitor large
54 boulders, thus improving resilience with respect to the additional hazards they pose.

55 Several techniques exist to monitor landslide movements, used also in the context of real time
56 extraction of displacements. For example, early warning systems have been based on traditional
57 techniques such as topographic benchmarks, or extensometers, often in combination with more
58 advanced techniques such as ground based radar interferometry (GB-InSAR) (e.g. Intrieri et al., 2012;
59 Loew et al., 2017). Geodetic techniques based on GPS or total stations are also widely used and
60 documented to remotely monitor surface displacements of active landslides (e.g. Glueer et al., 2019).
61 On one hand, traditional techniques tend to be cheaper but they only allow the retrieval of point-like
62 information and they can pose challenges for installation. On the other hand, advanced techniques
63 such as GB-InSAR allow for more continuous coverage but involve much higher costs related to both
64 equipment and data processing and cannot easily deliver information in real time. Wireless
65 technologies are desirable, due to unfavourable terrain conditions in which landslide monitoring is
66 often needed. In this respect, passive radio-frequency (RFID) techniques have recently been used to
67 monitor landslide displacements, and they have been shown to be inexpensive and versatile (Le
68 Breton et al., 2019). Although this type of technique has not yet been used in early warning systems,
69 it is contended that the adaptability of such technology could be developed in this context. The main
70 advantage is their low cost, their wireless nature and also the ability of the sensors to work in the
71 presence of adverse environmental factors, that would impair other techniques such as GPS and total



72 stations (e.g. fog, snow, dense vegetation). However, passive RFID tags currently allow for a
73 monitoring distance (distance between the tags and the receiving gateway) of a few tens of meters
74 only, which is disadvantageous when monitoring large unstable slopes or different geomorphic
75 settings in the same area, at the same time. None of the techniques mentioned above, however, have
76 been used to monitor boulder movement and most of them would not be suitable for this purpose
77 (perhaps with the exception of passive RFID), thus they have limited potential in capturing the
78 amplification of landslide hazard posed by the presence of large boulders.

79 Monitoring movement of sediments within floods has also received much attention in the literature.
80 For example, bedload transport can be monitored with environmental seismology, in order to detect
81 the seismic noise generated by moving particles (Burtin et al., 2011; Tsai et al., 2012). Whilst this is
82 useful in order to identify flood events, or even debris flows events in nearby tributaries, this is also
83 unsuitable for individual boulder monitoring. Passive radio sensor technology has been used to
84 monitor movement of individual grains in rivers (e.g. Bennett & Ryan, 2018; Bradley & Tucker, 2012),
85 however, this technique only allows the quantification of total transport distances between successive
86 surveys and no real-time data transmission has yet been achieved in this context. Several studies in
87 coastal settings have tracked individual boulders with extensive field surveys (e.g. Cox, 2020; Naylor
88 et al., 2016) giving insights into boulder dynamics. Similar efforts to track boulders in fluvial settings
89 are underway (e.g. Carr et al., 2018). However, such efforts are very time demanding and are also not
90 suited for real-time detection of boulder movement.

91 Recently, the use of IMUs (Inertial Measurement Unit) has been tested for different applications in
92 the field of geomorphology (e.g. Caviezel et al., 2018 and references therein). In particular, devices
93 able to capture boulder or pebble accelerations and rotations have been tested in different set-ups in
94 man-made environments. Gronz et al. (2016) have used devices equipped with a triaxial
95 accelerometer, a triaxial gyroscope and a magnetometer embedded within pebbles, to reconstruct
96 the path and movement of individual particles in a laboratory flume. Such devices, able to capture
97 accelerations up to 4g at 10 Hz, send data via an 868 MHz radio gateway from where it is then either



98 forwarded to a wireless router or directly downloaded to a computer via an Ethernet cable. Induced
99 rockfall field experiments were carried out in the Swiss Alps by Caviezel et al. (2018) in order to test
100 the applicability of IMUs to accurately measure boulder accelerations and rotations for the calibration
101 of rockfall models. The devices used in the latter study have high sampling frequency (1 kHz) and
102 acceleration detection range up to 400 g, the data is stored on a micro SD card and is then downloaded
103 via cable onto a computer. However, the lifetime of these sensors is limited by battery life (1 to 56
104 hours, depending on the settings types), hence requiring development to monitor, in field set-ups,
105 naturally occurring processes, that occur rarely and unpredictably.

106 In this study, we aim at filling a gap in the available literature regarding the monitoring of individual
107 boulders, in real-time and in different geomorphological settings in the field. In the context of the
108 possible future development of an early warning system, the priority of this pilot study is heavily
109 focused on capturing the activation of boulder movement in real-time, rather than on the accuracy
110 and precision of the measurement itself, the latter requiring further development. We explore how
111 displacements or even subtle orientation changes of boulders lying within a large, slow moving and
112 potentially deep-seated landslide body can be used to identify landslide reactivation and evolution of
113 the activity levels of different sectors through time. We contend that this ability may allow to
114 investigate landslide dynamics, geometries and failure modes in future developments and with denser
115 networks. Additionally, we explore how rapid boulder movement within active tributary channels
116 could indicate events such as debris flows, and their monitoring could help identify in the future the
117 energy thresholds required for remobilisation of different grain sizes. As mentioned above,
118 technologies that can work in real time and wireless are better suited for this purpose. For this reason,
119 in this work, we explore the transfer of a technology developed in the field of ecology to the
120 monitoring of boulders in slow moving landslides and debris flows. Wireless devices equipped with a
121 GPS module and an accelerometer originally developed for animal tracking, are modified and adapted
122 for the purpose of boulder tracking and monitoring. GPS trackers in combination with accelerometers
123 have been used to tag different animals in order to extract information on migratory, nesting and



124 feeding behaviours among other things (e.g. Soriano-Redondo et al., 2020; Panicker et al., 2019;
125 Gilbert et al., 2016). Whilst some trackers store the data internally and transmit it to a server via GSM
126 when a network becomes available, the trackers used for this study have been developed to allow for
127 a network of nodes that communicate wireless and in real time through an Internet of Things (IoT)
128 system (e.g. Panicker et al., 2019) that works with a gateway installed locally. In an IoT system, the
129 nodes of the network communicate to the gateway over radio frequencies and without the need for
130 human intervention. The gateway can then be directly connected to a computer or, crucially, it can
131 transmit the data via GSM network to a server in real time.

132 Transferring this type of technology to boulder monitoring brings several advantages in comparison
133 to other monitoring systems. The devices used in this work can be used to monitor several boulders
134 at the same time and in different geomorphological settings within a large study area, thanks to the
135 longer range achievable by the system in comparison to, for example, RFID techniques. Moreover, our
136 long-range wireless devices can be directly activated by movement and have real-time
137 communication, this potentially enabling us to 1) unravel landslide evolution and mechanics, provided
138 a dense enough network, and 2) develop an early warning system for hazardous events that involve
139 the presence of boulders.

140 In this study, based in the Upper Bhote Koshi catchment (red square in inset in Fig. 1), Nepal, we
141 demonstrate the use of long-range wireless devices to detect hazardous boulder movement and
142 landslide reactivation in real time. We also demonstrate for the first time the use of this technology
143 in the field of geomorphology, and in a field setup, to monitor the movement of boulders embedded
144 within a landslide and in two debris flow channels.

145 2. Study area

146 2.1. Hazards and their interactions in the area of study

147 Nepal lies at the heart of the Himalayan arc and it is one of the most disaster-prone countries in the
148 world. In particular, the extreme topographic gradients, seismicity and monsoonal climate, coupled



149 with increased population pressure (Whitworth et al., 2020), make Nepal widely and frequently
150 affected by landslides and various types of floods. In 2015 a large number of coseismic landslides were
151 triggered as a consequence of the Gorkha earthquake sequence, in particular in association with the
152 largest M 7.8 Gorkha earthquake (25 April 2015) and M 7.3 Dolakha earthquake (12 May 2015).
153 Several authors mapped coseismic landslides after the events and, although numbers vary greatly (a
154 few thousands to a few tens of thousands of landslides mapped in different studies), the impact from
155 these hazards has been unanimously recognised as very significant (Reynolds, 2018a,b; Roback et al.,
156 2018; Martha et al., 2017; Kargel et al., 2016). The Bhote Koshi catchment, northeast of Kathmandu
157 (red square in inset in Fig. 1), was also identified as one of the most affected areas, showing the
158 greatest density of landslides (Roback et al., 2018; Guo et al., 2017; Tanoli et al., 2017; Kargel et al.,
159 2016; Collins & Jibson, 2015). The areal distribution of landslides away from the main shock epicentre
160 appears to have been controlled by a combination of PGA, slope and fault rupture propagation
161 (Roback et al., 2018; Martha et al., 2017; Regmi et al., 2016). Some authors pointed out that many
162 coseismic landslides occurred at high elevations (e.g. Tanoli et al., 2017), and it was observed that
163 after the earthquake, a large number of landslides remained disconnected from the channels, with
164 significant amounts of material stored on the hillslopes (Cook et al., 2016; Collins & Jibson, 2015),
165 including boulders that are still visible today on valley flanks. During the 2015 monsoon, new
166 landslides were triggered along with the expansion of coseismic landslides, but loose material
167 remained stored on the hillslopes by the end of the monsoon (Cook et al., 2016). The sediments
168 produced with coseismic landslides are expected to move from the hillslopes and into the fluvial
169 system over several years after the earthquake (Collins & Jibson, 2015 and references therein).
170 The Bhote Koshi is also highly prone to glacial lakes outburst floods (GLOFs), with six events reported
171 since 1935 (Khanal, 2015). Different authors have mapped in recent years glacial lakes within the
172 Bhote Koshi catchment, the total number ranging between 74 and 122 (Khanal, 2015; Liu, 2020),
173 making glacial lake density in this catchment four times higher than that of the central Himalaya (Liu,
174 2020). All available studies are in agreement regarding the recent increase in the total area of glacial



175 lakes in the region, in relation to increasing temperatures and glacial retreat (Liu 2020), with some
176 authors suggesting that this increase amounts to 47% and that some lakes doubled in size between
177 1981 and 2001 (Khanal, 2015). Some of these lakes have the potential to drain catastrophically, with
178 some authors indicating that this risk may increase in the future, as glacial lakes increase in number
179 and volume. The floods originated from the outburst of glacial lakes can have short-lived discharges
180 that are several orders of magnitude higher than background discharges in receiving rivers (Cook et
181 al., 2018) and can have impacts for many tens of km downstream (Richardson & Reynolds, 2000; Huber
182 et al., 2020; Liu et al., 2020; Khanal et al., 2015). The latest one in the Bhote Koshi catchment occurred
183 in July 2016, likely originated from a rain-induced debris flow into Gongbatongshacuo Lake, a moraine-
184 dammed lake in Tibet (Autonomous Region of China) (Cook et al., 2018; Reynolds, 2018c), that drained
185 catastrophically impacting infrastructure and properties up to 40 km downstream. Boulders up to 8 m
186 long, weighing in excess of 150 tonnes, jammed the sluices gates of the Bhote Koshi Hydropower
187 project, diverting the debris-charged flash flood through and totally destroying the desilting basin,
188 inducing substantial damage to the site (Reynolds, 2018a). During the remedial works for the
189 reconstruction of the headworks infrastructure, a boulder with 17 m diameter (~4,500 tonnes) was
190 uncovered adjacent to the upstream wall of the headworks dam. This complex event has highlighted
191 the need for improved ways of understanding the interactions of cascading hydro-geomorphic
192 processes and to improve measures aimed at increasing resilience (Reynolds, 2018b,c). The availability
193 of loose material on hillslopes, the monsoonal climate and the GLOFs hazard in the area, enhance the
194 possibility of material containing large grain sizes to reach the river network via hillslope movements,
195 and eventually be remobilised by exceptionally large floods. Huber et al. (2020) highlight that very
196 large boulders (~10 m in diameter) present today in the Bhote Koshi river have likely been transported
197 by large GLOFs events, supporting the idea that it is unlikely that monsoon generated floods may have
198 the energy threshold required to remobilise very large grain sizes (Cook et al., 2018).

199 Landslides and debris flows can occur also as a consequence of heavy and persistent rainfall during
200 the monsoon. Every year the area receives up to 4100 mm of rainfall between June and September



201 (Tanoli et al., 2017). Active monsoons can trigger or reactivate landslides, an example is the Jure
202 landslide (roughly 15 km southwest of our study sites) occurred in August 2014 (Acharya et al., 2016).
203 Moreover, intense monsoon rainfall events can trigger debris flows in low order streams channels
204 within the region (Roback et al., 2018), this allowing for movement of some smaller boulders (> 0.25
205 m diameter) and allowing hillslope-channel coupling.

206 *2.2. Geologic and tectonic setting*

207 Our study sites lie within the Main Central Thrust (MCT) zone (Rai et al., 2017), where the rocks of the
208 Higher Himalaya Sequence (HHS) are thrust over rocks of the Lesser Himalaya Sequence (LHS). The
209 MCT is one of the main faults that accommodate the subduction of the Indian subcontinent under the
210 Eurasian Plate. The MCT has been mapped at the top and bottom of the ~350 m thick Hadi Khola Schist
211 that is sandwiched between the Dhad Khola Gneiss above and the Robang Phyllite below at Tatopani,
212 some 5 km upstream of the study site (DMG, 2005, 2006; Rai, 2011; Reynolds, 2018b). The study site
213 lies entirely within the Benighat Slate, which comprises predominantly black schist, phyllite, quartzite
214 and carbonate rocks (DMG, 2005,2006; Rai, 2011). The rocks belonging to the HHS are composed by
215 crystalline, amphibolite to granulite facies metamorphic rocks, mainly ortho- and paragneisses,
216 quartzite and schists. The LHS rocks present lower grade metamorphism, increasing towards the MCT,
217 and are largely comprised of phyllites, schists, metasandstones and quartzites (Basnet & Panthi, 2019;
218 Martha et al., 2017; Rai et al., 2017; Upreti, 1999; Gansser, 1964).

219 *2.3. Economic assets in the study area – increased vulnerability*

220 Our study sites are located along the Araniko Highway, a major route that connects Kathmandu to
221 Kodari and then links Nepal to China. This main road was significantly affected by earthquake induced
222 landslides in 2015, but is also subjected to landslides every year during the monsoon season (e.g.
223 Whitworth et al., 2020). The area is of strategic importance for Nepal due to the high concentration
224 of hydropower projects, either already in operation or under construction (Khanal et al., 2015).
225 Moreover, the Araniko Highway is a key trade and transport link (Liu et al., 2020) and one of the two



226 routes between China and Nepal. Khanal et al. (2015) indicate that International trade and tourism
227 between Nepal and China have been growing rapidly since the opening of the Araniko Highway and
228 that this route is economically important, with the records of the Customs Office in Nepal showing a
229 value of US\$ 135.9 million in imports and US\$ 4.1 million in exports in 2011/2012, with both
230 governments benefiting from the revenue.

231 *2.4. Selected sites*

232 The study site is located at the northern edge of an inferred deep seated gravitational slope
233 deformation around 1.5 km wide that stretches from Hindi in the north to just upstream of Chakhu to
234 the south (Reynolds, 2018b). A secondary landslide body on the northwest-facing valley flank directly
235 impinging the settlement of Hindi, and two debris flow channels were chosen as tagging sites (Fig. 1).
236 The most active debris flow channel of the two marks the northeastern boundary of the landslide,
237 whilst the other channel, which appears to be less active, is located 360 m to the northeast, directly
238 upstream of the densest part of the settlement of Hindi. Both channels intersect the Araniko highway
239 and cross the settlement before merging with the Bhote Koshi. The landslide is a soil slide covering an
240 area of approximately 0.03 km². Colluvium material likely deposited from previous landslides is visible
241 at the headscarp and in the terraces along the southwestern flank, with the presence of large boulders
242 of diameter > 2 m. Large boulders are also observed scattered over the landslide body. The scarp
243 suggests a depth of the landslide of at least 2 m, and large, fresh cracks were observed in the crown
244 area in October 2019, indicating activity during the previous monsoon season.

245 **3. Methodology**

246 *3.1. Network setup and components*

247 Twenty-three long range wireless smart sensors, complying with the LoRaWAN® (Long Range Wide
248 Area Network) specification, provided with external GPS and LoRa antennae and measuring 23 mm by
249 13 mm (Fig. 2B), were used as nodes in the system. The sensors are equipped with an accelerometer
250 configured to sample at 2 Hz, as well as a GPS module. When movement is detected by the



251 accelerometer, so that tilt or acceleration exceed defined thresholds, collection of GPS and
252 accelerometer data is activated. In the absence of movement, the devices are programmed to record
253 and transmit one single location per day at a fixed time. The sensors, which were developed by
254 Movetech Telemetry and Miromico, transmit the acquired data to a LoRaWAN® gateway on the 868
255 MHz band wirelessly and in real time. A Multitech IP67 LoRaWAN® gateway, sends the payloads
256 received from the sensors to a Loriot LoRaWAN® network server through the local GSM network using
257 an agnostic SIM card (Fig.2A-D). The packages are then sent from Loriot to the Movetech Telemetry
258 server and are decoded providing the raw information collected by the nodes.

259 Each sensor was fitted with one (Fig. 2B) or two Lithium C-cells batteries connected in parallel. Twenty-
260 three boulders were individually tagged by embedding the sensors in a hole drilled in the rock (Fig.
261 2C). Each boulder was drilled with a 35 mm core drill, for a length of about 15 cm. The depth of the
262 hole allowed for the emplacement of the C-cell batteries and the sensor. After placement, each hole
263 was filled with epoxy resin, sealing the cavity, thus protecting the device from tampering and from the
264 elements, whilst allowing for unaffected connectivity to the gateway via LoRa.

265 The position of the gateway, located in the opposite side of the valley at a distance of about 800 m
266 from the sensors, at 1330 m a.s.l. and roughly 60 m above the valley bottom was chosen to be within
267 reach of the GSM network and have direct line of sight with the sensors (Fig. 1 and 2E). Due to
268 unreliable mains power supply, a 4-panels solar system was developed for this purpose. The initial set-
269 up did not allow for continuous power to the gateway and led to instability in the system with frequent
270 offline times during the 2019 monsoon season. However, the system has been improved and it will
271 guarantee continuous power to the gateway for successive acquisition seasons. The panels currently
272 charge two 12 V, 110 AH batteries that then provide continuous power to the gateway through a POE
273 (power over ethernet) supply. The solar system is composed by parts that can be sourced locally, at
274 relatively low cost and that can be transported to sites without road access, such as the site chosen in
275 this study. The nature of the local GSM network, relying on one individual antenna in the area at the
276 time of this study, has also led to frequent GSM connection failures which prevented the gateway



277 from communicating with the server. The devices deployed in the 2019 season were programmed to
278 not store the data, but to send it immediately, causing the data transmitted during gateway offline
279 time to be lost.

280 3.2. Choice of tracked boulders

281 The tagging sites were selected with the aim of covering different geomorphological settings whilst
282 retaining visibility to the gateway. The boulders identified for tagging are spread over three sites, two
283 debris flow channels and a landslide body (Fig. 1). The boulders cover a range of sizes and geologies,
284 though the geology in this context is not expected to play a significant role in affecting the connectivity
285 of the network. The smallest boulders tagged have b-axis of 0.3 m, whilst the largest boulder has a b-
286 axis of 3.3 m (Appendix 1). The selected boulders are characterised by differences in their position at
287 their location. Boulder location and embedment influenced the choice of the accelerometer settings
288 used, as explained in the section below. They can be subdivided into three categories: in channel (IC),
289 partly embedded (PE) and fully embedded (FE) either within the landslide body or in the channel banks
290 (Fig. 3 and Appendix 2). Boulders in the channel are expected to move freely in case of a large event,
291 and to be potentially subjected to collisions. Such event could be a debris flow with sufficient intensity
292 to impart forces high enough to cause the boulder to move downslope within the flow. Fully
293 embedded boulders are not expected to move independently of the surrounding soil mass, as such,
294 they can only move coherently with the material on channel banks or with landslide body if these
295 were to undergo sliding episodes and reactivation. For these boulders, generally only the top part is
296 visible, whilst the bottom is fully surrounded by soil. On the other hand, partly embedded boulders,
297 found at the headscarp, along the southwestern flank of the landslide or in the channel banks, can
298 either move coherently with the surrounding material or become dislodged and begin to move freely
299 on the surface. The second scenario is related to the little amount of soil covering the bottom part,
300 particularly in the downslope direction, and this scenario would occur if the soil were to be eroded
301 during intense rainfall events.



302 3.3. *Sensors settings*

303 The sensors were programmed to send a routine message every 24 hours. As mentioned in section
304 3.1, the sensors can also acquire and send data in association with an accelerometer event for which
305 activation thresholds can be set for impact forces and for angular variations. The sensors can be
306 programmed following two main modes: 1) the accelerometer data is averaged over a window of time
307 (over a number of recordings), we call this mode “*average*” settings (AVG in Appendix 2) and 2) the
308 absolute value of the maximum acceleration occurring in a time interval can be recorded, and we call
309 this mode “*maximum*” settings (MAX in Appendix 2). In the first case, the values of the three axes are
310 normalised and the measurements essentially represent the static angle of tilt or inclination, thus the
311 projection of the acceleration of gravity, g , on the three axes, ranging between 0 (for a horizontal axis)
312 and ± 1 (for a vertical axis). In the second case, the absolute maximum value can be recorded and this
313 can exceed 1 g and can be set to be as high as 2, 4, 8 or 16 g. The measurement resolution changes
314 according to the chosen detectable maximum, so that a scale capped at 2 g has a resolution of 0.016
315 g, whilst a scale capped at 16 g has a resolution of 0.186 g (Appendix 3).

316 For an individual axis, the variation in the accelerometer values would correspond to an angular
317 change as shown in Eq. (1):

318

$$319 \quad \gamma = \arcsin(m/1000) * 180^\circ/\pi \quad (1)$$

320

321 where γ is the angular variation on a given axis and m is accelerometer value recorded on the same
322 axis in g. According to Eq. (1), if the scale is capped at 2 g, for $m = 0.016$ g the corresponding angular
323 variation is of $\sim 0.9^\circ$ if the axis is vertical, but $\sim 5.5^\circ$ if the axis approaches horizontal. Similarly, if the
324 scale is capped at 16 g, $m = 0.186$ g corresponds to an angular variation of about 10° when the axis is
325 near-vertical, but this increases to as high as $\sim 21^\circ$ when the axis approaches the horizontal (Appendix
326 3). As a consequence of the different resolutions, we observed acquisitions of data triggered by small



327 variability in accelerometer measurements around a stable value, rather than true movement, with
328 this effect becoming more important in sensors programmed with the coarser scale.

329 The boulders expected to move coherently with the soil in which they are embedded, and that are
330 more likely to experience small and gradual angular variations as the surrounding material gently
331 slides, were programmed with the *average* settings. We chose to cap accelerometer data for average
332 settings at 2 g, as high impact forces were not expected, and we assigned thresholds for activation on
333 accelerometer events of ~ 0.4 g and 5° for impact forces and angular changes respectively. The sensors
334 in the two debris flow channels and some of those only partly embedded within the landslide were
335 programmed to record high impact forces using the *maximum* settings (Appendix 2). In this case, the
336 scale was capped at the maximum detectable force of 16 g and the impact and angular thresholds
337 were set at ~ 4 g and 5° respectively. This angular threshold yielded noisier data with respect to the
338 sensors programmed with the *average* settings type, because of the direct consequence of a drastic
339 reduction in measurement resolution (Appendix 3). Measurement variability and errors related to the
340 sensors led to spurious data, given the relatively small angular threshold assigned for the highest
341 detectable maximum of 16 g. In other words, given that the step of accelerometer measurement is as
342 high as 0.186 g, a spurious angular variation of more than 5° is often detected even when the boulder
343 is stable, due to intrinsic measurement variability (up to 2 bits).

344 In order to reduce the noise in the data due to these fluctuations, a three-stages smoothing is applied
345 to the raw data. First, a moving window covering 5 successive data points is used. The median value
346 of the 5 data points is assigned to all points in the window that lie within ± 0.186 g of the data point
347 immediately before the window. If any of the values lie outside the ± 0.186 g threshold, then the raw
348 data points are left unchanged. In the second stage, peaks of one data point are removed (i.e. one
349 point above or below two points with the same value), this is because if a high impact force is imparted
350 to a boulder, the position of the boulder is expected to change. This would mean that a high value
351 would likely be followed by a change in the static angle of tilt of the three axes. Therefore, it is
352 unrealistic to have a peak value followed by a value equal to that observed before the peak. In the



353 third and final stage, another moving window of 5 consecutive data points searches for values that lie
354 within ± 0.186 g threshold with respect to the last point immediately before the window. The same
355 value of the last point before the window is assigned if all points are within the threshold. If any of the
356 points lie outside of the ± 0.186 g threshold, the values are left unchanged.

357 The sensors are equipped with a GPS module, which is currently also used to retrieve the date and
358 time of the data acquisition, whilst the data transmission has another timestamp related to the arrival
359 of the data string to the server. The accelerometer readout in the current version of the software is
360 tied to a GPS acquisition, this means that although the accelerometer is measuring as soon as
361 movement is detected, the acquisition is obtained only when the GPS has successfully retrieved the
362 position. An acquisition of accelerometer data with no GPS position can be obtained and transmitted
363 (in which case it would only be associated with a server timestamp), but only after the GPS has
364 attempted to retrieve the position and failed. The timeout for the GPS search has been set to 120
365 seconds. This is because due to the local topographic settings, the availability of enough satellites at a
366 given time may be low. During this time, no accelerometer acquisition can be recorded and
367 transmitted in the current firmware version of the devices, although development has already been
368 made to separate the accelerometer acquisition from the GPS for future acquisition seasons.

369 *3.4. Validation data*

370 A Bushnell NatureView HD camera was installed at the gateway location. The camera was set to
371 acquire an image every 30 minutes and the field of view included the landslide and the southwestern
372 debris flow channel to around 35 m below the Araniko Highway. Given the rugged terrain and the line
373 of sight, the visibility in the area around the southwestern flank of the landslide is limited and the
374 observation is best for the lower part of the slope. Image cuts were performed for analysis over the
375 visible parts of the southern channel and of the landslide (Fig. 1). Pixels visually recognisable in all
376 image frames were selected. These correspond to individual trees or boulders and were identified in
377 successive frames. This allowed for a rough estimate of the displacements of these features in the
378 image plane through the available image sequence.



379 Moreover, the landslide body and the southwestern channel (Fig. 1) were scanned with a Faro Focus
380 3D X330 terrestrial laser scanner (TLS) in two successive campaigns in April and in October 2019. Each
381 site was scanned from two scan locations and the point clouds were aligned by matching stable areas
382 using the Multistation Adjustment algorithm in Riegl RiSCAN Pro (v. 2.3.1). The data were analysed to
383 obtain ground displacements during the monsoon season, and processed using the point-to-point
384 cloud comparison method M3C2 in CloudCompare (Lague et al., 2013). Field camera and TLS data
385 were used to identify days characterised by sliding of the landslide body, sliding of the channel banks,
386 boulder movements and areas that underwent significant changes of the ground surface. This data is
387 used in a qualitative way for comparison with and validation of the accelerometer data obtained with
388 the wireless devices and, despite the qualitative approach, this data provided a quite detailed
389 overview of the days in which movement occurred. Two Pe6B 3-component geophones recording at
390 200 Hz were installed on fluvial terraces below the study site to monitor debris flow activity in the
391 debris flow channels (Burtin et al., 2009).

392 4. Results

393 We observed that during the 2019 monsoon season, there were important sliding episodes of the
394 main landslide body, which caused small and gradual tilt of the tagged boulders embedded within it.
395 Moreover, although there is no evidence of large debris flows in either of the channels tagged (for
396 example in the seismometer record), some boulders within the southern channel bounding the
397 landslide show data that could indicate rapid movement. Of the 23 boulders tagged, nine show
398 accelerometer time series that are compatible with downslope movement (yellow to red symbols in
399 Fig. 4). Of these, six lie within the landslide body and were programmed with the *average* settings in
400 order to detect small angular changes (Fig. 5). The remaining three were located within the southern
401 debris flow channel and were programmed with the *maximum* settings, to capture large (> 1 g)
402 impacts (Fig. 6).



403 In terms of boulder sizes, boulders that appeared to have moved within the landslide have b-axes
404 ranging from 0.4 to 2.75 m, whilst those that moved in the southern channel have b-axes comprised
405 between 0.4 and 0.5 m (Appendix 1), thus covering a much smaller range.

406 The 4 boulders within the landslide that do not show evidence of movement (white circles in Fig. 4),
407 were fitted with sensors programmed with the *maximum* settings (Appendix 2), due to the fact that
408 they are partly embedded in the landslide and to the potential to become detached from the landslide
409 body, and thus given the lower accuracy and coarser scale they could not have detected small, gradual
410 movements even if they had been subjected to them.

411 *4.1 Slow movements within the landslide body*

412 The movement recorded by boulders embedded within the landslide body is consistent with slow,
413 gradual tilting that occurred coherently with the sliding of the landslide mass. Small rotational
414 components of the displacement vector that can either be related to the whole mass or, most likely,
415 to different sectors of the landslide, induce small angular variations to the boulders embedded within
416 the soil, at the surface. Figure 5 shows the accelerometer data for fully or partly embedded boulders
417 programmed with the *average* settings. An interpretation of this type of movement, related to gentle
418 tilting of the boulder within the soil mass, is shown in panels A and B in Fig. 5. The data shows that all
419 sensors that detected movement were appropriately charged throughout the season. Time is shown
420 on the x axis, from 15 May 2019 to 31 Oct 2019, whilst the y axis indicates the value of the projection
421 of g on each accelerometer axis in mg (g^{-3}). The values of each axis are recalculated to show the
422 deviation from the original position for visualisation purposes, rather than the actual values measured
423 (hence all raw data curves begin at 0, and the smoothed curves around zero, due to the smoothing).
424 The variations of the accelerometer axes from the original position range from 10 mg to 200 mg in the
425 different sensors. For an individual axis, the variation in the values would correspond to an angular
426 change as shown in Eq. (1). Thus, for $m = 10$ mg , $\gamma \cong 0.6^\circ$ and $\gamma \cong 8^\circ$ for a near horizontal and near
427 vertical axis respectively and for $m = 200$ mg , $\gamma \cong 12^\circ$ and $\gamma \cong 37^\circ$ in the horizontal and vertical cases.
428 In all boulders the rotation is oblique with respect to all axes and does not occur around any of them.



429 The images acquired by the timelapse camera (a video is provided in supplements), indicate that the
430 landslide moved slowly at the beginning of the rainy season and then accelerated later in the season,
431 most likely in relation to an increase in the pore water pressure within the soil. This temporal evolution
432 is also observed in our accelerometer data. Moreover, it is likely that the landslide is divided in sectors
433 with different activity levels and different response to rainfall through time (e.g. Bonzanigo, 2021). In
434 particular, Fig. 4 and 5 show that the movements of boulders within the landslide not only differ in
435 the magnitude of the angular variations recorded, which is an order of magnitude higher for B# A226
436 and B# 9A41 in comparison to other boulders, but also in the evolution with time. Three boulders (B#
437 33EB, not shown in Fig. 5, B# F3CE and B# 5B6A, the positions of which are also labelled in Appendix
438 2) show movements early in the time series, already during May and June. The other three boulders
439 (B# 96F2, B# A226 and B# 9A41) show a later onset of the movement between late August and mid-
440 September. The boulders with early movements are located below the main scarp (B# F3CE) and in
441 the middle part of the landslide (B# 33EB and B# 5B6A), closer to the channel, whilst those that move
442 later are closer to the southwestern flank of the landslide (B# 9A41 and B# 96F2), thus farther away
443 from the channel, and in the lower half of the landslide body (B# A226).

444 Visual interpretation of the images acquired by the field camera (section 3.4) indicates that significant
445 movements of the landslide body occurred during sliding episodes within the orange hatched area in
446 Fig. 4. The area in which visible changes occurred is about 5000 m² and corresponds to the lower
447 portion of the landslide. Fig. 5H indicates the estimated movement magnitudes in the image plane for
448 the lower, medium and upper parts of the visible sliding area (indicated by L, M, U in Fig. 4).
449 Displacements of up to ~2 m in the image plane are detected in the lower and mid-slope parts of the
450 moving area (Fig. 5H and 7A) between the end of August and the beginning of September. The
451 movement observed in the accelerometer data of B# A226 and B# 9A41 (Fig. 5F-G) corresponds to the
452 periods in which higher displacement magnitudes are inferred from the images. Fig. 4 and Fig. 7B also
453 show that boulders B# 5B6A, B# 33EB and B# 9A41 are located in areas surrounded by displacements
454 as seen by the TLS data (yellow hatched areas in Fig. 4). Moreover, two boulders within the upper part



455 of the landslide were not found in the field campaign carried out in October 2019 (B# 33EB and B#
456 625C), likely due to fresh accumulation of material from the scarp. Indeed, TLS scan data show
457 cumulative displacements of up to 1 m over large areas between April and October 2019 (Fig. 7).

458 *4.2 Rapid orientation changes of boulders in the southern debris flow channel*

459 Fig. 6 shows the accelerometer data obtained for boulders located within the southern debris flow
460 channel or on its banks, between 15 May 2019 and 22 October 2019. The difference in the scale of the
461 accelerometer output with respect to Fig. 5 is explained by the different settings. These boulders were
462 programmed to retrieve actual g values (as opposed to normalised values) and forces up to 16 g. The
463 raw data (grey curves) shows frequent oscillations often within ± 0.186 g around a value
464 (corresponding to one step in the accelerometer scale, or one bit) and occasionally up to ± 0.372 g
465 (two steps in the scale, two bits), associated with measurement variability and the coarse scale used
466 (Section 3.3).

467 As an example, in the graph for B# 4C02, we observe a change from the initial position equivalent to
468 1000 mg in y and around 700 mg in x and z. This is compatible with a change between the initial
469 position (1) and position 2, attained by the boulder by 4 June 2019, as visualised in Fig. 6B. The current
470 settings have not captured how the boulder transitioned between position 1 and position 2, likely due
471 to the very short time interval during which the change is expected to have happened. The GPS
472 acquisition is likely to have taken longer than the movement that triggered the recording and delayed
473 the accelerometer acquisition. This applies to the other two boulders shown in Fig. 6. We do not
474 observe forces > 1 g for any of the sensors programmed with the *maximum* settings, despite the ability
475 of the sensors to detect up to 16 g. This is consistent with a lack of debris flow activity recorded by
476 cameras or seismometers, the more prolonged activity of which would have generated sustained
477 boulder movement, beyond the time needed for GPS acquisition as explained below.

478 Fig. 6G shows rainfall data (daily and cumulative) from GPM IMERG (Bolvin et al., 2015) in green, while
479 the orange bars indicate days in which movement (sliding of the banks and/or individual boulder
480 movement) is observed within the channel in the images acquired by the field camera. Often periods



481 with movement observations occur after days of moderate to intense and/or persistent rainfall. B#
482 4C02 shows movement data recorded by the accelerometer as early as beginning of June. Even though
483 this is early in the monsoon season, this movement falls within a few days of moderate rainfall at the
484 beginning of June during which movements in the channel are already visible in the camera's images.
485 Similarly, B# 57B9 and B# FB58 show movement (i.e. changes in orientation) that are very close in time
486 to periods for which other movements are visible within the channel in the images. An example of
487 boulder movement that occurred roughly 25 m downstream of the tagging area is shown in Fig. 8A-B,
488 whilst Fig. 8C shows the areas on the northeastern channel bank and the channel bed for which
489 significant changes in the ground surface during the monsoon season are detected with the TLS data.
490 The vertical green bars in the graphs of B# 57B9 and B# FB58 (Fig. 6C and E) show the uncertainty
491 regarding the timing of the recorded movements. Essentially, each green bar indicates a window of
492 time during which the movement observed may have occurred. The data of each orientation change
493 marked by a green bar may have been transmitted at a different time from the acquisition time, as
494 explained below. An explanation of the different scenarios that are described below is also given in
495 the flowchart in Fig. 9. The position change of B# 4C02, the second event of B# 57B9 and the first event
496 of B# FB58 are characterised by equal GPS timestamp (time of acquisition) and server timestamp (time
497 of transmission). This indicates that the data transmission occurred within seconds of the data
498 acquisition. B# 57B9 shows two changes in orientation between 26 and 30 July 2019. The sensor
499 experienced a gap in the GPS timestamp between 06:15 UTC on 22 July and 06:21 UTC on 28 July, as
500 the GPS failed to obtain a position during this time. Moreover, during this period the gateway went
501 temporarily offline. Due to these reasons, it impossible to know whether the movement that cause
502 the orientation change shown in the data transmitted on 26 July occurred immediately before
503 transmission or during the window for which the GPS timestamp is not available. The gateway
504 experienced another offline period between 09:36 UTC on 28 July and 03:51 UTC on 30 of July, by
505 which time the data shows that an orientation change has occurred. Although the acquisitions have



506 both GPS and server timestamps and these are the same (i.e. acquisitions sent in real time), the actual
507 movement may have happened at any time between those two timestamps.

508 During the period encompassing the two recorded movements (26 – 30 July), the field camera images
509 indicate overcast, rainy conditions that corresponded with important sliding of the right bank of the
510 channel, offering supporting evidence for movement within the channel. B# FB58 sent data from 15
511 August 2019 up to 07:17 UTC on 24 August 2019 regularly (based on the server timestamp) but
512 without a GPS time stamp. A small gap follows, due to the gateway being offline, from 07:17 UTC on
513 24 August until 16:00 UTC on 25 August, by when the change of orientation has occurred and the GPS
514 and server time stamp are the same (data sent in real time). Thus, the second movement of B# FB58
515 is likely to have occurred between these two times, even if the data acquired after the gateway was
516 online again has been sent in real time on 25 August. The camera images show that movements on
517 the right bank of the channel occur between 22 and 24 August. The scan data also shows important
518 displacements in the channel right bank (Fig. 8C). Moreover, 5 boulders in the channel (or on the bank)
519 were not found in October 2019 at their original location. Two of these are boulders that appear to
520 have moved in the smart sensors' data and the other three may have been covered by deposition of
521 loose material.

522 No boulder movement was recorded for the northern channel, and field observations in October 2019
523 revealed no signs of recent activity in the channel, which was completely overgrown with vegetation.

524 *4.3 GPS module limitation*

525 The GPS had an overall poor performance across all the sensors during the data acquisition season.
526 The average success rate of GPS acquisition (the ratio between the number of acquisitions with GPS
527 time stamp and all acquisitions) for the 23 sensors is ~49%, with two sensors never acquiring a GPS
528 position throughout the time they have been active. Moreover, the standard deviation of positions
529 ranges between 4.3 m and 15.8 in the x and 5.5 m and 22.6 m in y after removing outliers. The GPS
530 data acquired is unrealistic not only for the magnitude of the position differences of the same boulder,
531 but also because the direction is often inverted in time, which is not compatible with possible boulder



532 movement. However, the poor performance of the GPS for the purpose of boulder tracking has only
533 limited impact on the ability to detect movement or orientation changes using the accelerometer, as
534 outlined in the previous sections.

535 5. Discussion

536 Our data show that nine out of 23 sensors emplaced in boulders at our tagging sites have transmitted
537 data compatible with real boulder movement, this indicating the potential of the technology used for
538 detecting both gradual angular variations and changes in boulder orientation associated with rapid
539 movements in real time. This result, based on the first deployment of this network, is very promising
540 for the use of this technology in early warning systems in the future, because it shows that the onset
541 of movement can be identified in real time, provided that all components of the network operate
542 correctly.

543 The movements observed for the boulders scattered on the landslide body and embedded within the
544 material can be described as small angular variations that occurred gradually during the season. Visual
545 recognition of such movements in the field or in the camera images and scan data would be unfeasible
546 for individual boulders because they correspond only to small tilt that is difficult to detect with such
547 methods. However, there are elements that support the fact that the data acquired by the
548 accelerometer is real and caused by gradual tilting. The images acquired by the cameras show
549 important sliding of the landslide in August-September (Fig. 7A), when the boulders located around
550 the southwestern flank and in the lower part of the landslide show higher magnitude of the angular
551 variations with respect to other boulders (Fig. 5F-G). The fact that the onset of movement observed
552 in six boulders in the landslide is not random but follows a spatial and temporal pattern also supports
553 the idea of a landslide reactivation that causes smaller movements around the headscarp and nearer
554 the channel to occur earlier. The headscarp activity may not only be related to the movement of the
555 entire mass, but also to small collapses of the colluvium material in the steep exposure. This may have
556 led to small movements already from the onset of the monsoon. Movements in this area are



557 supported by data obtained with the TLS that indicate that displacements in the line of sight of up to
558 1 m occurred at or just below the headscarp during the season (Fig. 7B). Moreover, two boulders in
559 this area were not found in October 2019, most likely because they have been covered by recent
560 collapses of loose material from the headscarp. The area near the northeastern flank may have
561 experienced an increase in pore pressures due to earlier saturation of the soil here than in the area at
562 the opposite flank, also related to a more rapid increase of the ground water table nearer the channel
563 driven by topography. We also observe that the magnitude of movements of boulders closer to the
564 southwestern flank and in the lower slope is higher than elsewhere; this is well supported by
565 observations obtained through the field camera.

566 Four partly embedded boulders in the landslide (Appendix 2) were programmed with the *maximum*
567 settings and showed no movement (Fig. 4). The reason to choose this setting type for these boulders
568 is that the nature of their position (PE) may have led to larger and faster downslope movements if
569 they had become dislodged. Given the lower resolution of the data obtainable from the *maximum*
570 settings, it is possible that nothing is observed for these boulders even if they moved consistently with
571 the landslide body and experienced tilting of a few degrees. In other words, it is possible that such
572 boulders also moved but that the nature of the movements may have been too subtle to be captured
573 with the settings applied. It is also possible that these boulders found themselves outside of the active
574 sectors of the landslide, although this seems less likely given the observations obtained in the field
575 and also from camera images and scan data.

576 Another element that supports the fact that the recorded accelerometer data is associated with real
577 boulder movement is related to boulder size. Appendix 1 shows boulder sizes for boulders with and
578 without movement in the three different tagging sites. For boulders within the landslide body, a size
579 control on movement was not anticipated. This is because boulders were expected to move
580 coherently with the landslide mass and thus their potential to be transported would be independent
581 from their size. On the contrary, in the channel, and particularly for boulders lying in the channel bed,
582 a size control on movement is expected, because the size of boulders that could be mobilised by a



583 flow depends on the flow intensity (Clarke, 1996). Therefore, a flow with low intensity could not be
584 expected to mobilise the largest boulders tagged. The observations indicate that boulders that show
585 movements in the landslide are characterised by a much higher range of b-axes than those in the
586 channel (Appendix 1).

587 For boulders programmed with the *maximum* settings, we observed noisier accelerometer data than
588 for those programmed with the *average* settings. What controls this behaviour is not the fact that the
589 sensors were programmed to detect the maximum force or the static tilt respectively, but rather the
590 scale that was chosen and associated with the two settings types. As mentioned before, 16 g and 2 g
591 were chosen as values to cap the scale in the *maximum* and *average* settings respectively.

592 When a sensor is programmed to be capable of capturing forces impacting a boulder as high as 16 g,
593 the resolution currently available for the accelerometer's reading is of 0.186 g. Although this is a
594 relatively small value with respect to 16 g, this corresponds to an angular variation of 10.7°. Moreover,
595 we observe that measurement variability is often 1 bit, but occasionally 2 bits, the latter corresponding
596 to 0.372 g and an angular variation of 21.8°. As the sensors can be activated on both an angular
597 threshold or an impact threshold detected on any of the axes, care must be taken when selecting the
598 angular threshold in relation to the achievable accuracy. An angular threshold of 5° at this resolution
599 is below the measurement error and can trigger a large amount of spurious data strings. This has the
600 negative effect of diluting the signal with noise and, crucially, to reduce battery lifetime. The downside
601 of programming sensors with the settings for high impacts recording is that small angular variations
602 cannot be detected. Future improvements of the accelerometer accuracy, resulting for example from
603 the activation of the 9-axes IMU present in the hardware of the devices, could reduce this problem.

604 Although the GPS module is expected to produce readings with a positional error of less than 2 m in
605 normal conditions, we observed a significant increase in the standard deviation of the measurements
606 in northing and easting. This could be caused by three effects: 1) the narrow valley drastically reduces
607 the visibility time of any passing satellites and thus the chances that a suitable number of satellites
608 will be available to each sensor for calculating the position; 2) the GPS is activated relatively rarely and



609 this may reduce accuracy (and thus in time precision) of the obtained positions; 3) the rock in which
610 the sensors are embedded appears to deteriorate the signal. Experiments carried out at the sites have
611 shown that even sensors placed outside of a boulder, held in the open air and away from obstacles,
612 needed several minutes to get a GPS position. Moreover, experiments carried out in the UK, at an
613 open site, have shown that the same sensors at the same site retrieved a position within a radius of
614 ~50 m when placed inside a boulder and within a radius of ~2 m when held in the open air. The
615 acquisition of a GPS position is also what causes the largest battery expenditure in the sensors and it
616 is therefore detrimental for long-term data acquisition on boulder movement. The high positional
617 errors and the important battery expenditure make the current GPS module not fit for the purpose of
618 tracking boulders in rugged terrains.

619 As mentioned above, it is possible to retrieve data strings from the sensors without a GPS timestamp.
620 So, even if a GPS position, date and time cannot be acquired, the accelerometer data can be recorded
621 and transmitted anyway, with the server timestamp. In this sense, the fact that the accelerometer was
622 tied to the GPS during the 2019 acquisition season, so that the accelerometer data could be recorded
623 only once the GPS acquisition has been attempted and failed, did not invalidate completely the data
624 output.

625 However, there are also important limitations related to this. As the time for the GPS acquisition
626 attempt was set to 120 seconds, the sensor measures the acceleration already during this time, but it
627 does not record it nor transmit it until the GPS position is either acquired or fails. In the case of fast
628 movements, or relatively large impacts caused by the sudden movements of boulders within the flow,
629 120 seconds (this would often be even more, in case a GPS acquisition is being obtained) may be
630 enough time for the movement to begin and stop. This may explain why, although the boulders in the
631 channel were programmed to detect high forces, they never show accelerometer values higher than
632 1 g (either negative or positive). In essence, these sensors have also only recorded the static tilt and
633 different orientations acquired by the boulders in time, but not the actual movement as it unfolded.
634 For instance, the position change of B# 4C02, B# 57B9 (second event, i.e. event that causes transition



635 from position 2 and 3) and B# FB58 (first event, i.e. event that causes transition from position 1 and
636 2) were received in real time. This means that as soon as the data string indicating a different
637 orientation with respect to the previous data string was acquired, it was also sent. In this type of
638 situation, the GPS timestamp is the same as the server timestamp, but there is no recording of the
639 movement as it unfolded. The event of B# 4C02 points to the fact that the GPS delayed the acquisition
640 of the accelerometer data, because the gateway was online during the time in which the orientation
641 change must have occurred. Given that there is no evidence of large debris flows during the 2019
642 monsoon season, B# 4C02 may just be one example of minor boulder movement that started and
643 stopped within the ~120 seconds time interval. This may be improved in successive acquisition
644 seasons, since development has been made in order to separate the GPS from the accelerometer
645 acquisitions. The next batch of devices that will be deployed in the network will thus be able to capture
646 faster rotation already from the start of the movement.

647 The picture may be complicated even further by the fact that occasionally the gateway experienced
648 some offline time, due either to the battery not being recharged properly or to GSM connection loss.
649 This is the case of B# 57B9 (second event) and B# FB58 (first event), in which we observe that the data
650 string indicating an orientation change is sent in real time, but follows a gap in the gateway
651 connectivity. In this case, the movement may have occurred at any point during the offline period of
652 the gateway, then the first acquisition since the gateway became once again online is sent in real time.
653 However, a new solar system is now in place and will prevent future power issues during future
654 acquisition seasons.

655 *5.1 Advantages and limitations of this technology*

656 The LoRaWAN® smart active sensors developed in this study for the purpose of identifying boulder
657 movements has already shed light on its potential advantages and its limitations. The technology used
658 is independent of weather conditions. The communication between the tags and the gateway is not
659 hampered by adverse weather conditions and movements were observed during overcast and rainy
660 days. This is of course true if the gateway is powered with batteries of sufficient capacity to withstand



661 days with insufficient sunlight, which may occur during the monsoon season. Although a good visibility
662 of the sensors from the gateway increases connectivity between the nodes and the gateway, the long-
663 range nature of the system allows for a network that extends over a relatively large area. In our case,
664 we were able to obtain data from boulders located at up to 800 m from the gateway, covering an area
665 of about 0.25 km², this likely not being the upper limit of the achievable range. This is especially
666 advantageous for a number of reasons. Different geomorphic features can be monitored with the
667 same gateway, in our case including a landslide and two debris flow channels. Moreover, in
668 comparison with other innovative and promising techniques such as passive RFID technology (Le
669 Breton et al., 2019), which can currently allow for a range of about 60 m, our network offer the
670 advantage of covering different sectors of the main landslide, in case of large unstable areas, thus not
671 limiting the observation to restricted sectors, which could offer a more complete picture of the
672 instability dynamics. Moreover, the long range of our devices can allow to increase the monitoring
673 area further, thus potentially enabling us to identify movement further upstream in the monitored
674 channels, which is essential to provide enough lead time to secure operations at major infrastructure
675 sites or to alert downstream populations.

676 An important characteristic of the devices used in this study as opposed with other techniques is that
677 they are active and can easily be assigned thresholds (e.g. acceleration or tilt) that can be used in an
678 early warning system context. Moreover, the devices can be embedded directly inside boulders,
679 without the need for additional supports that may 1) make the devices more visible/exposed and thus
680 more subjected to intentional tampering or animal damage, 2) there is no additional movement to be
681 accounted for (e.g. tilting of supporting poles). The technology is also relatively low cost and has the
682 potential to become competitive and cost-effective in the future. The most expensive component is
683 the gateway (~1000 USD), whilst the devices are around 200 USD each. The ability to retrieve the tags
684 after battery consumption has already been investigated and will be implemented in successive
685 acquisition seasons, will allow for a durable, cost-effective network. This may make this technology



686 more affordable than other more expensive techniques such as GB-InSAR, GPS or total stations and
687 can allow dense networks.

688 The main drawback encountered in this study is the poor performance of the GPS module, which made
689 it impossible to directly evaluate the magnitude of displacements either of the landslide or of
690 individual boulders. Measurements of displacement are ideally needed to understand landslide
691 velocity changes in time and space for example in response to climatic forcing (e.g. Handwerger et al.,
692 2019; Bennett et al., 2016) as well as to identify the acceleration of a landslide towards failure (e.g.
693 Carlà et al., 2019; Handwerger et al., 2019). Moreover, the GPS acquisition, tied to the recording of
694 accelerometer data, has hampered in some cases the ability to obtain the full sequence of
695 accelerations experienced by the boulders. This issue will however be resolved in the next acquisition
696 season, since further development has allowed us to make the accelerometer independent of GPS
697 acquisitions. Work is also planned to write the firmware to enable the gyroscope and magnetometer
698 on the device, which will give more detail of boulder dynamics such as rotations. Finally, the
699 connectivity of the gateway to the server (during offline periods) has prevented some of the time the
700 ability to receive the movement signal in real time. This problem has now been resolved, with a more
701 stable solar system currently powering the gateway, thus future acquisition seasons should benefit of
702 higher robustness and less connectivity loss.

703 **6. Conclusions**

704 We show the application of a smart sensor LoRaWAN® network for the detection of boulder
705 movements within a landslide and a debris flow channel in the Upper Bhoite Koshi catchment
706 (northeastern Nepal). We tagged 23 boulders ahead of the 2019 monsoon season with devices
707 equipped with an accelerometer and able to send data in real time to a LoRaWAN® gateway. Of these
708 23 boulders, nine sent data compatible with movement. Six of these were fully or partly embedded in
709 a soil slide and are characterised by accelerometer time series that indicate slow, gradual angular
710 variations. Such angular variations reflect the coherent movement of boulders within the landslide



711 mass. The reactivation of the landslide is confirmed by both timelapse cameras and TLS data. Also, the
712 movements show staggered onset, so that the boulders nearer the scarp or the lower boundary, near
713 the channel, began to move earlier in the season than other boulders. In the channel, only three
714 boulders show data likely corresponding to sharp, sudden movements and rotations that occurred in
715 response to intense or persistent rainfall. The sizes of the boulders that moved in the channel are
716 towards the smallest end of the boulders tagged in the channel, reflecting the fact that no large debris
717 flows were observed in the channel during the 2019 monsoon season.

718 Though with some limitations, the technology has proven able to detect boulder movements with this
719 type of device, for the first time in a field setup as opposed to a laboratory setup. In the optimal
720 conditions of all the component of the network operating properly, the ability to capture the onset of
721 movement in real-time is an important premise to the use of this technology in early warning systems
722 of slope movements that involve the presence of hazardous boulders. This pilot study also hints at the
723 potential of these devices to further understanding of landslide dynamics, for example the timing of
724 movement in response to rainfall and the spatial sequencing of movement across a landslide. The
725 most important challenge that we believe has prevented the recording of the complete movement for
726 the boulders in the channel is related to the current requirement for a GPS position to be acquired for
727 the accelerometer data to be recorded and transmitted. Furthermore, the poor GPS performance
728 currently precludes the measurement of displacement of the landslide. However, the sensors are
729 already equipped with a 9-axis IMU comprising an accelerometer, a gyroscope and a magnetometer,
730 that have not been ready for the field tests in Nepal, but that in the future are expected to replace the
731 need for an accurate GPS.

732 Future work will involve the tagging of more boulders at the same sites of the current network to
733 improve the accelerometer sampling frequency, the now improved the stability of the network
734 connectivity, more suitable programming settings and the ability to retrieve and reuse the tags. In the
735 next batch of devices, we will be able to activate the accelerometer and record movement data
736 independently of the GPS acquisition. This is expected to significantly speed up data acquisition and



737 transmission to the server, which will be a step forward in view of using this technology for early
738 warnings. Moreover, this will also allow us to capture the whole accelerations sequence associated
739 with fast rotations induced by large impact forces and may enhance the understanding of boulder
740 movement from the hillslopes into the river network.

741 **Acknowledgments**

742 This work was carried out as part of the BOULDER project, funded by the NERC/SHEAR Catalyst
743 program (NE/S005951/1). Nick Griffin carried out essential work related to powering the devices and
744 setting up the solar system. Gareth Flowerdew indefatigably carried out the drilling, essential for
745 embedding the devices in the boulders. Phil Atkinson has contributed to this work by helping decoding
746 the raw data and managing SIM card usage of the gateway. Shuva Sharma and Pawan Timsina from
747 Scott Wilson Nepal (SWN) provided support during the initial phases of the work, network installation
748 and helped organising dissemination workshops for the project. Bhairab Sitaula's contribution to
749 logistical and technical aspects of the field campaigns was essential. Bibek Raj Shreshta contributed to
750 boulder tagging and Joshua Jones helped finding the tagged boulders after the monsoon. Luc Illien
751 helped placing the seismometers for detection of debris flows for validation of our data. Alan Rae and
752 Stephen Drewett provided support related to the LoRaWAN® server and the gateway. Stephen
753 Laycock at UEA shared a code to visualise our accelerometer data and the orientation changes with a
754 model boulder.

755

756 **Author Contributions**

757 B.D. tested and programmed the sensors, analysed the data and wrote the paper; G.L.B. shaped the
758 idea, wrote the proposal obtaining funding for this work and contributed to the data analysis; A.M.F.
759 tested and programmed the sensors and contributed to the data analysis. B.D., G.L.B., A.M.F. and
760 M.R.Z.W. carried out field work and network installation. C.L.K. installed the seismometers, carried
761 out the two scans of the area and contributed to the analysis of the scan data. A.S. carried out software



762 development and participated to field work. J. M. R. contributed to the original idea of the project. All

763 authors revised and made contributions to the manuscript.

764

765 **Competing Interests statement**

766 The authors declare no competing interests.

767

768



769 7. References

- 770 Acharya, T. D., Mainali, S. C., Yang, I. T. and Lee, D. H.: Analysis of jure landslide dam, Sindhupalchowk
771 using GIS and Remote Sensing, *Int. Arch. Photogramm. Remote Sens. Spat. Inf. Sci. - ISPRS Arch.*, 41,
772 201–203, doi:10.5194/isprsarchives-XLI-B6-201-2016, 2016.
- 773 Basnet, C. B. and Panthi, K. K.: Evaluation on the Minimum Principal Stress State and Potential Hydraulic
774 Jacking from the Shotcrete-Lined Pressure Tunnel: A Case from Nepal, *Rock Mech. Rock Eng.*, 52(7),
775 2377–2399, doi:10.1007/s00603-019-1734-z, 2019.
- 776 Bennett, G. L. and Ryan, S.: Rock and Roll: Passive sensing of fluvial bedload and wood transport and
777 interaction, *Eguga*, 18272, 2018.
- 778 Bennett, G. L., Roering, J. J., Mackey, B. H., Handwerger, A. L., Schmidt, D. A. and Guillod, B. P.: Historic
779 drought puts the brakes on earthflows in Northern California, *Geophys. Res. Lett.*, 43(11), 5725–5731,
780 doi:10.1002/2016GL068378, 2016a.
- 781 Bennett, G. L., Miller, S. R., Roering, J. J. and Schmidt, D. A.: Landslides, threshold slopes, and the survival
782 of relict terrain in the wake of the Mendocino Triple Junction, *Geology*, 44(5), 363–366,
783 doi:10.1130/G37530.1, 2016b.
- 784 Bolvin, D. T., Braithwaite, D., Hsu, K., Joyce, R., Kidd, C., Nelkin, E. J., Xie, P., Huffman, G., Bolvin, D. T.,
785 Braithwaite, D., Hsu, K., Joyce, R., Kidd, C., Nelkin, E. J. and Xie, P.: NASA Global Precipitation
786 Measurement (GPM) Integrated Multi-satellitE Retrievals for GPM (IMERG) Prepared for: Global
787 Precipitation Measurement (GPM) National Aeronautics and Space Administration (NASA), Algorithm
788 Theor. Basis Doc. Version 4.5, 4(November), 26 [online] Available from:
789 https://pmm.nasa.gov/sites/default/files/imce/times_allsat.jpg%0Ahttps://pmm.nasa.gov/sites/default/files/document_files/IMERG_ATBD_V4.5.pdf%0Ahttps://pmm.nasa.gov/sites/default/files/document_files/IMERG_ATBD_V4.5.pdf, 2015.
- 792 Bonzanigo, L.: The Landslide of Campo Vallemaggia, in *World Geomorphological Landscapes*, pp. 379–
793 386, Springer., 2021.
- 794 Le Breton, M., Baillet, L., Larose, E., Rey, E., Benech, P., Jongmans, D., Guyoton, F. and Jaboyedoff, M.:
795 Passive radio-frequency identification ranging, a dense and weather-robust technique for landslide
796 displacement monitoring, *Eng. Geol.*, 250, 1–10, doi:10.1016/j.enggeo.2018.12.027, 2019.
- 797 Burtin, A., Bollinger, L., Cattin, R., Vergne, J. and Nábělek, J. L.: Spatiotemporal sequence of Himalayan
798 debris flow from analysis of high-frequency seismic noise, *J. Geophys. Res. Earth Surf.*, 114(4),
799 doi:10.1029/2008JF001198, 2009.
- 800 Burtin, A., Cattin, R., Bollinger, L., Vergne, J., Steer, P., Robert, A., Findling, N. and Tiberi, C.: Towards the
801 hydrologic and bed load monitoring from high-frequency seismic noise in a braided river: The “torrent
802 de St Pierre”, French Alps, *J. Hydrol.*, 408(1–2), 43–53, doi:10.1016/j.jhydrol.2011.07.014, 2011.
- 803 Carlà, T., Intrieri, E., Raspini, F., Bardi, F., Farina, P., Ferretti, A., Colombo, D., Novali, F. and Casagli, N.:
804 Author Correction: Perspectives on the prediction of catastrophic slope failures from satellite InSAR
805 (Scientific Reports, (2019), 9, 1, (14137), 10.1038/s41598-019-50792-y), *Sci. Rep.*, 9(1), 1–9,
806 doi:10.1038/s41598-019-55024-x, 2019.
- 807 Carr, J. C., DiBiase, R. A., Yeh, E. C., Carr, J. C., DiBiase, R. A. and Yeh, E. C.: High resolution UAV surveys of
808 bedrock rivers in Taiwan reveal connections between lithology, structure, and channel morphology,
809 in *Agufm*, vol. 2018, pp. T23A-0340., 2018.
- 810 Caviezel, A., Schaffner, M., Cavigelli, L., Niklaus, P., Bühler, Y., Bartelt, P., Magno, M. and Benini, L.: Design
811 and Evaluation of a Low-Power Sensor Device for Induced Rockfall Experiments, *IEEE Trans. Instrum.*
812 *Meas.*, 67(4), 767–779, doi:10.1109/TIM.2017.2770799, 2018.
- 813 Clarke, A. O.: Estimating probable maximum floods in the Upper Santa Ana basin, Southern California,
814 from stream boulder size, *Environ. Eng. Geosci.*, 2(2), 165–182, doi:10.2113/gsegeosci.ii.2.165, 1996.
- 815 Collins, B. D. and Jibson, R. W.: Assessment of Existing and Potential Landslide Hazards Resulting from the
816 April 25, 2015 Gorkha, Nepal Earthquake Sequence (ver.1.1, August 2015) U.S. Geological Survey
817 Open-file Report 2015-1142, US Geological Survey., 2015.
- 818 Cook, K., Andermann, C., Adhikari, B., Schmitt, C. and Marc, O.: Post-earthquake modification of 2015



- 819 Gorkha Earthquake landslides in the Bhote Koshi River valley, Eguga, EPSC2016-9482, 2016.
- 820 Cox, R.: Megagravel deposits on the west coast of Ireland show the impacts of severe storms, *Weather*,
821 75(3), 72–77, doi:10.1002/wea.3677, 2020.
- 822 Gansser, A.: *Geology of the Himalayas*. Regional Geology Series, Wiley, London., 1964.
- 823 Gilbert, N. I., Correia, R. A., Silva, J. P., Pacheco, C., Catry, I., Atkinson, P. W., Gill, J. A. and Aldina, A. M.:
824 Are white storks addicted to junk food? Impacts of landfill use on the movement and behaviour of
825 resident white storks (*Ciconia ciconia*) from a partially migratory population, *Mov. Ecol.*, 4(1), 7,
826 doi:10.1186/s40462-016-0070-0, 2015.
- 827 Glueer, F., Loew, S., Manconi, A. and Aaron, J.: From Toppling to Sliding: Progressive Evolution of the
828 Moosfluh Landslide, Switzerland, *J. Geophys. Res. Earth Surf.*, 124(12), 2899–2919,
829 doi:10.1029/2019JF005019, 2019.
- 830 Gronz, O., Hiller, P. H., Wirtz, S., Becker, K., Iserloh, T., Seeger, M., Brings, C., Aberle, J., Casper, M. C. and
831 Ries, J. B.: Smartstones: A small 9-axis sensor implanted in stones to track their movements, *Catena*,
832 142, 245–251, doi:10.1016/j.catena.2016.03.030, 2016.
- 833 Guo, C. wen, Huang, Y. dan, Yao, L. kan and Alradi, H.: Size and spatial distribution of landslides induced
834 by the 2015 Gorkha earthquake in the Bhote Koshi river watershed, *J. Mt. Sci.*, 14(10), 1938–1950,
835 doi:10.1007/s11629-016-4140-y, 2017.
- 836 Handwerger, A. L., Fielding, E. J., Huang, M. H., Bennett, G. L., Liang, C. and Schulz, W. H.: Widespread
837 Initiation, Reactivation, and Acceleration of Landslides in the Northern California Coast Ranges due to
838 Extreme Rainfall, *J. Geophys. Res. Earth Surf.*, 124(7), 1782–1797, doi:10.1029/2019JF005035, 2019.
- 839 Huber, M., Lupker, M., Gallen, S., Christl, M. and Gajurel, A.: Timing of exotic, far-travelled boulder
840 emplacement and paleo-outburst flooding in the central Himalaya, *Earth Surf. Dyn. Discuss.*, 1–29,
841 doi:10.5194/esurf-2020-17, 2020.
- 842 Intrieri, E., Gigli, G., Mugnai, F., Fanti, R. and Casagli, N.: Design and implementation of a landslide early
843 warning system, *Eng. Geol.*, 147–148, 124–136, doi:10.1016/j.enggeo.2012.07.017, 2012.
- 844 Kargel, J. S., Leonard, G. J., Shugar, D. H., Haritashya, U. K., Bevington, A., Fielding, E. J., Fujita, K.,
845 Geertsema, M., Miles, E. S., Steiner, J., Anderson, E., Bajracharya, S., Bawden, G. W., Breashears, D. F.,
846 Byers, A., Collins, B., Dhital, M. R., Donnellan, A., Evans, T. L., Geai, M. L., Glasscoe, M. T., Green, D.,
847 Gurung, D. R., Heijnen, R., Hilborn, A., Hudnut, K., Huyck, C., Immerzeel, W. W., Jiang, L., Jibson, R.,
848 Kääh, A., Khanal, N. R., Kirschbaum, D., Kraaijenbrink, P. D. A., Lamsal, D., Liu, S., Lv, M., McKinney, D.,
849 Nahirnick, N. K., Nan, Z., Ojha, S., Osenholler, J., Painter, T. H., Pleasants, M., Pratima, K. C., Yuan, Q.
850 I., Raup, B. H., Regmi, D., Rounce, D. R., Sakai, A., Shangguan, D., Shea, J. M., Shrestha, A. B., Shukla,
851 A., Stumm, D., Van Der Kooij, M., Voss, K., Wang, X., Weihs, B., Wolfe, D., Wu, L., Yao, X., Yoder, M. R.
852 and Young, N.: Geomorphic and geologic controls of geohazards induced by Nepal's 2015 Gorkha
853 earthquake, *Science (80-.)*, 351(6269), doi:10.1126/science.aac8353, 2016.
- 854 Khanal, N. R., Hu, J. M. and Mool, P.: Glacial lake outburst flood risk in the Poiqu/Bhote Koshi/Sun Koshi
855 river basin in the Central Himalayas, *Mt. Res. Dev.*, 35(4), 351–364, doi:10.1659/MRD-JOURNAL-D-15-
856 00009, 2015.
- 857 Lague, D., Brodu, N. and Leroux, J.: Accurate 3D comparison of complex topography with terrestrial laser
858 scanner: Application to the Rangitikei canyon (N-Z), *ISPRS J. Photogramm. Remote Sens.*, 82, 10–26,
859 doi:10.1016/j.isprsjprs.2013.04.009, 2013.
- 860 Liu, M., Chen, N., Zhang, Y. and Deng, M.: Glacial lake inventory and lake outburst flood/debris flow
861 hazard assessment after the gorkha earthquake in the Bhote Koshi Basin, *Water (Switzerland)*, 12(2),
862 464, doi:10.3390/w12020464, 2020.
- 863 Loew, S., Gschwind, S., Gischtig, V., Keller-Signer, A. and Valenti, G.: Monitoring and early warning of the
864 2012 Preonzo catastrophic rock slope failure, *Landslides*, 14(1), 141–154, doi:10.1007/s10346-016-
865 0701-y, 2017.
- 866 Martha, T. R., Roy, P., Mazumdar, R., Govindharaj, K. B. and Kumar, K. V.: Spatial characteristics of
867 landslides triggered by the 2015 Mw 7.8 (Gorkha) and Mw 7.3 (Dolakha) earthquakes in Nepal,
868 *Landslides*, 14(2), 697–704, doi:10.1007/s10346-016-0763-x, 2017.
- 869 Nathan Bradley, D. and Tucker, G. E.: Measuring gravel transport and dispersion in a mountain river using



- 870 passive radio tracers, *Earth Surf. Process. Landforms*, 37(10), 1034–1045, doi:10.1002/esp.3223, 2012.
- 871 Naylor, L. A., Stephenson, W. J., Smith, H. C. M., Way, O., Mendelssohn, J. and Cowley, A.:
872 Geomorphological control on boulder transport and coastal erosion before, during and after an
873 extreme extra-tropical cyclone, *Earth Surf. Process. Landforms*, 41(5), 685–700,
874 doi:10.1002/esp.3900, 2016.
- 875 Panicker, J. G., Azman, M. and Kashyap, R.: A LoRa Wireless Mesh Network for Wide-Area Animal
876 Tracking, in *Proceedings of 2019 3rd IEEE International Conference on Electrical, Computer and
877 Communication Technologies, ICECCT 2019*, pp. 1–5, IEEE., 2019.
- 878 Rai, S. M., Yoshida, M., Upreti, B. N. and Ulak, P. Das: Geology of the Lesser and Higher Himalayan
879 sequences along the Bhotekoshi River section between Syabru Besi and Rasuwa Gadhi (Nepal- China
880 border) area, central Nepal Himalaya, *Bull. Nepal Geol. Soc.*, 34(April), 2017.
- 881 Regmi, A. D., Dhital, M. R., Zhang, J. qiang, Su, L. jun and Chen, X. qing: Landslide susceptibility assessment
882 of the region affected by the 25 April 2015 Gorkha earthquake of Nepal, *J. Mt. Sci.*, 13(11), 1941–1957,
883 doi:10.1007/s11629-015-3688-2, 2016.
- 884 Reynolds, J. M.: Integrated Geohazard Assessments in high mountain environments : examples from the
885 Hindu Kush-Karakoram- Himalayan Region, in *Proceedings of ASIA*, pp. 1–8, Da Nang, Vietnam., 2018.
- 886 Roback, K., Clark, M. K., West, A. J., Zekkos, D., Li, G., Gallen, S. F., Chamlagain, D. and Godt, J. W.: The
887 size, distribution, and mobility of landslides caused by the 2015 Mw7.8 Gorkha earthquake, Nepal,
888 *Geomorphology*, 301, 121–138, doi:10.1016/j.geomorph.2017.01.030, 2018.
- 889 Shobe, C. M., Bennett, G. L., Tucker, G. E., Roback, K., Miller, S. R. and Roering, J. J.: Boulders as a lithologic
890 control on river and landscape response to tectonic forcing at the Mendocino triple junction, *GSA Bull.*,
891 doi:10.1130/b35385.1, 2020.
- 892 Soriano-Redondo, A., Acácio, M., Franco, A. M. A., Herlander Martins, B., Moreira, F., Rogerson, K. and
893 Catry, I.: Testing alternative methods for estimation of bird migration phenology from GPS tracking
894 data, *Ibis (Lond. 1859)*, 162(2), 581–588, doi:10.1111/ibi.12809, 2020.
- 895 Tanoli, J. I., Ningsheng, C., Regmi, A. D. and Jun, L.: Spatial distribution analysis and susceptibility mapping
896 of landslides triggered before and after Mw7.8 Gorkha earthquake along Upper Bhote Koshi, Nepal,
897 *Arab. J. Geosci.*, 10(13), 277, doi:10.1007/s12517-017-3026-9, 2017.
- 898 Tsai, V. C., Minchew, B., Lamb, M. P. and Ampuero, J. P.: A physical model for seismic noise generation
899 from sediment transport in rivers, *Geophys. Res. Lett.*, 39(2), doi:10.1029/2011GL050255, 2012.
- 900 Upreti, B. N.: An overview of the stratigraphy and tectonics of the Nepal Himalaya, *J. Asian Earth Sci.*,
901 17(5–6), 577–606, doi:10.1016/S1367-9120(99)00047-4, 1999.
- 902 Whitworth, M. R. Z., Moore, A., Francis, M., Hubbard, S. and Manandhar, S.: Building a more resilient
903 Nepal - The utilisation of the resilience scorecard for Kathmandu, Nepal following the Gorkha
904 Earthquake of 2015, *Lowl. Technol. Int.*, 21(4), 229–236, 2020.
- 905
906

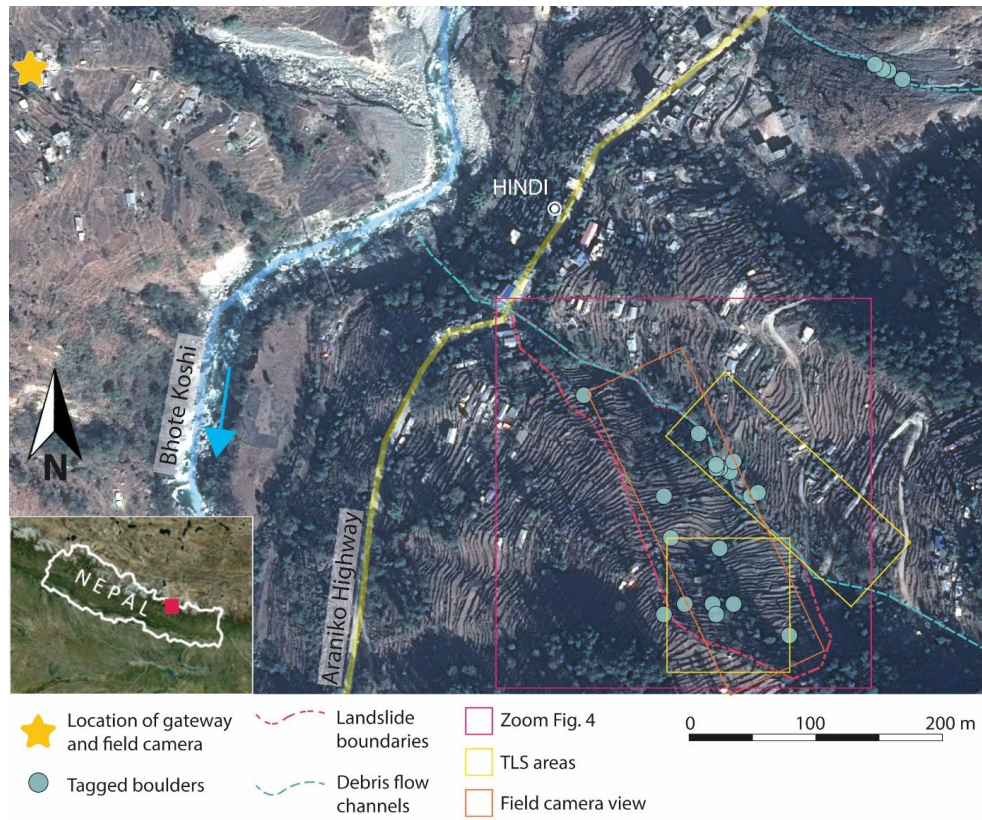


Fig. 1. Overview of study area and network, including three tagged sites (two debris flow channels and a landslide body). Red box, zoom of two tagged sites. Yellow boxes, terrestrial laser scanner areas. Orange box, field view of field camera. Image: Pleiades (CEOS Landslides Pilot).

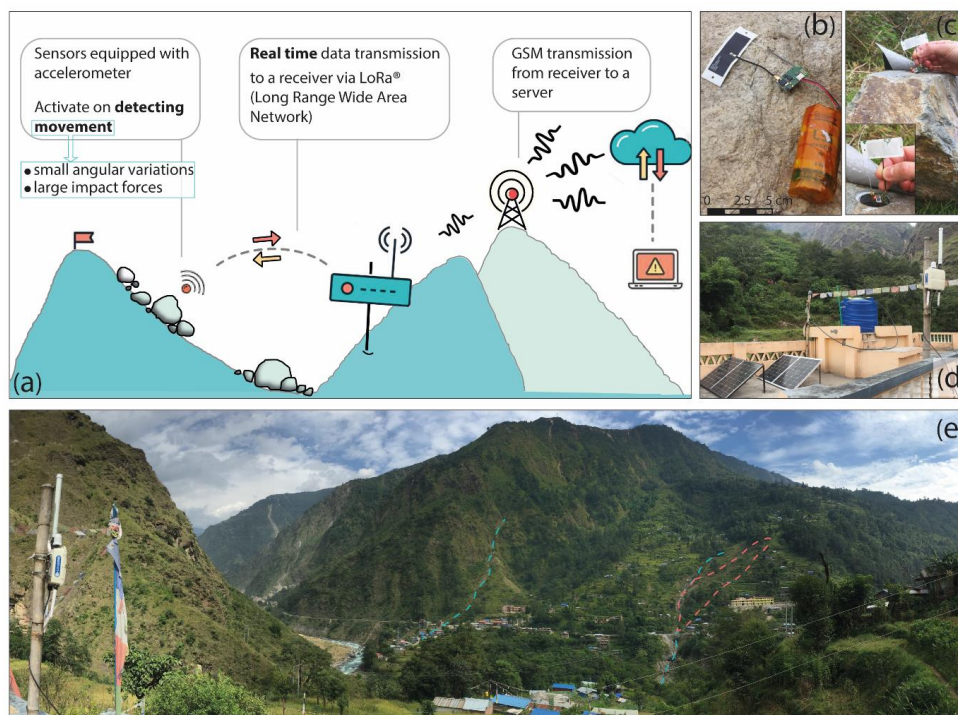


Fig. 2. A) Sketch of the network, its components and communication methods. B-C) Sensor and tagging of a boulder. D) Gateway setup. E) Overview of the tagging sites from the gateway. Gateway visible in the far left of the image. Blue dashed lines mark the debris flow channels and red dashed lines mark the boundaries of the landslide.

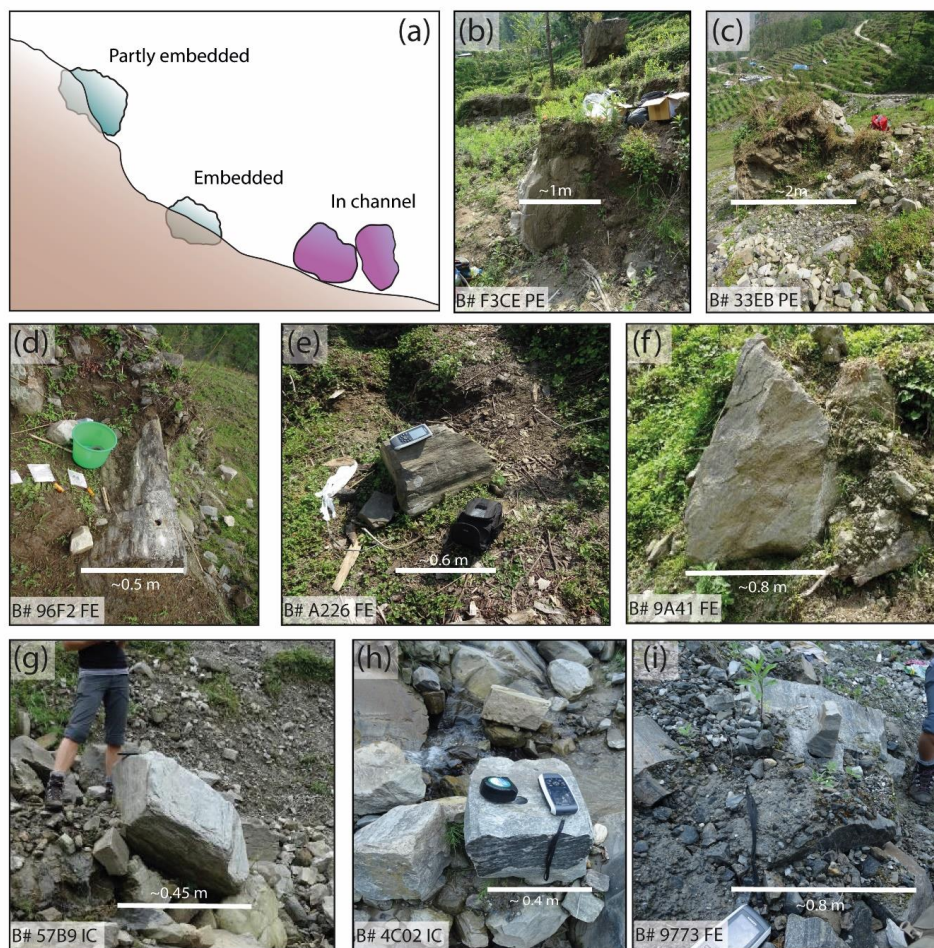


Fig. 3. A) Sketch of boulder position types. B-C) Examples of partly embedded (PE) boulders within the landslide body. D-E-F) Examples of fully embedded (FE) boulders within the landslide body. G-H) Examples of boulders inside the main channel (IC). I) Example of fully embedded (FE) boulder within the channel bank.

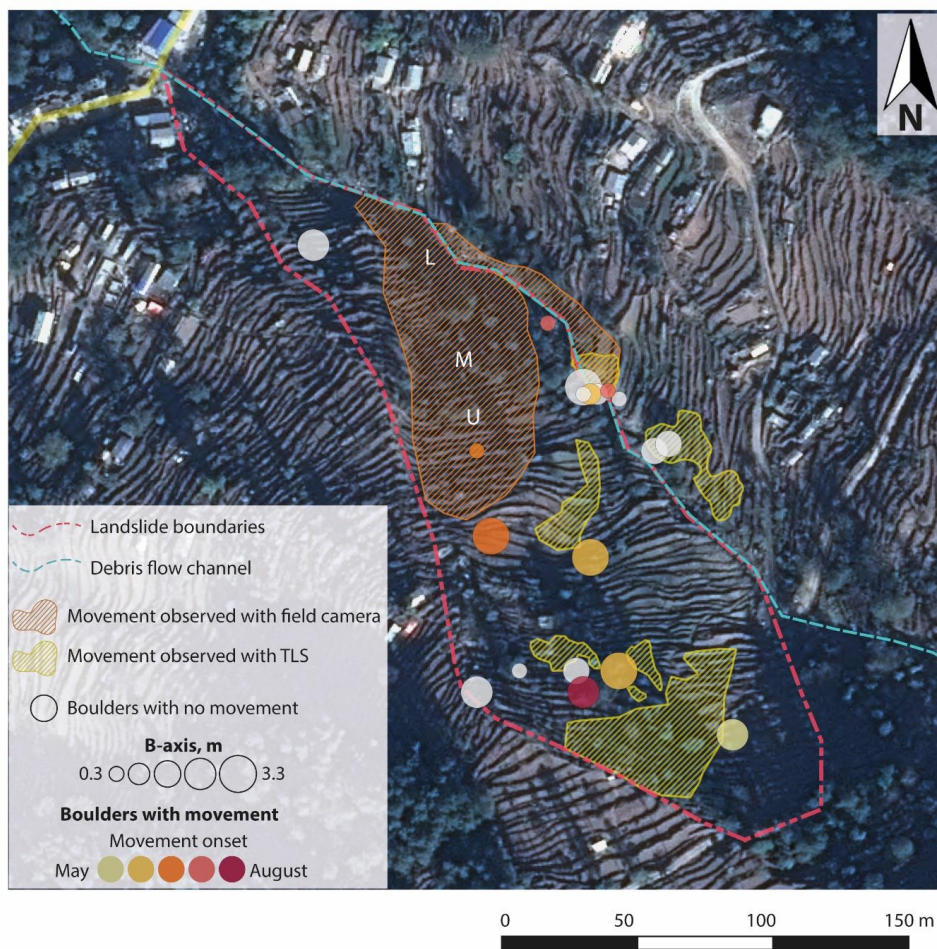


Fig. 4. Zoom of two tagged sites. The sizes are scaled according to the b-axis of the boulders (example of scales given for boulders without movement in legend but applies to all boulders). White squares are boulders that did not move or for which movement was not recorded. Green circles are boulders in the debris flow channel. Yellow to red symbols are boulders within the landslide body. Hatched areas are zones with observed movement through images (L: lower, M: mid-slope, U: upper), and terrestrial laser scanning. Image: Pleiades (CEOS Landslides Pilot).

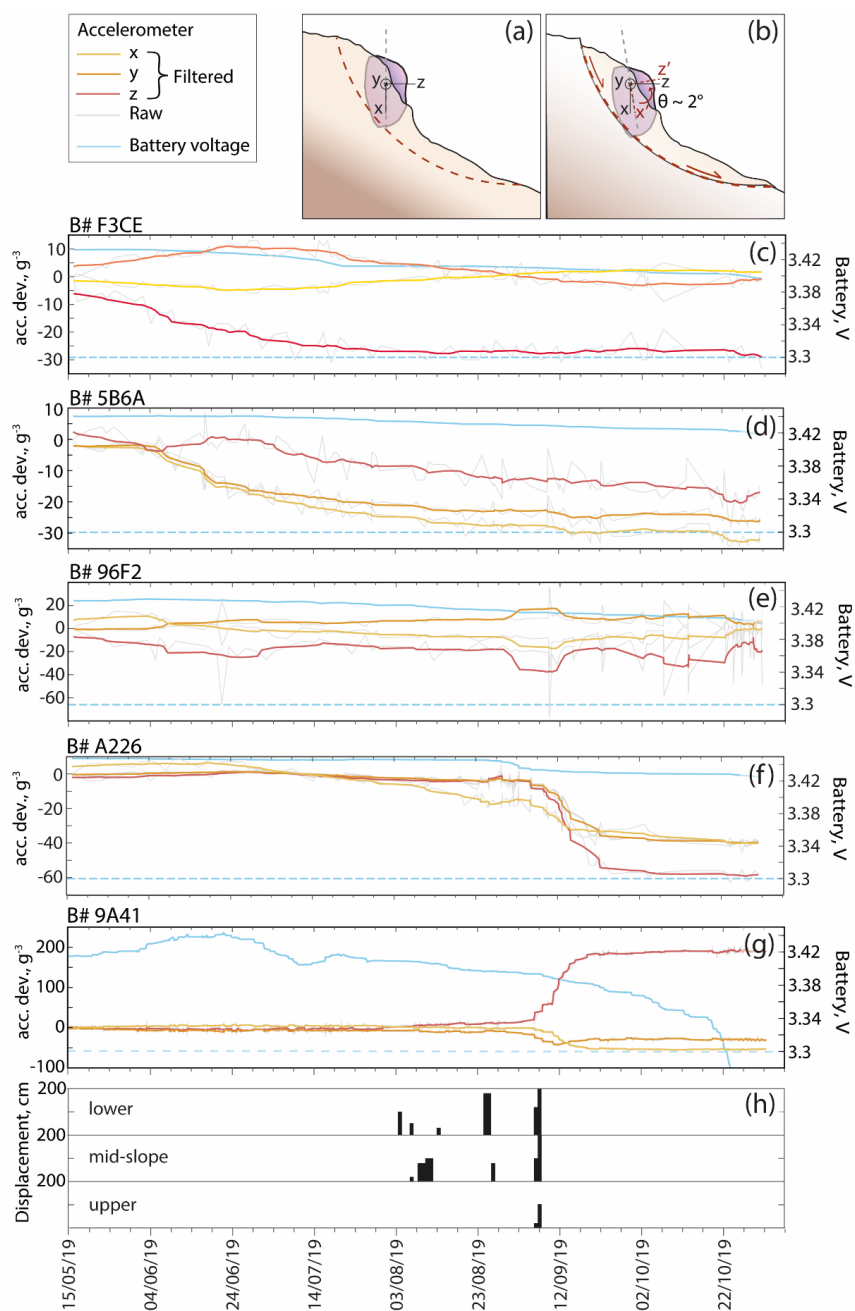


Fig. 5. Accelerometer data deviation from initial position for boulders within the landslide body through the monsoon season. A-B) Sketch of possible movement of embedded or partly embedded boulders. C) Estimated displacements of lower, mid-slope and upper parts of the slope obtained through field camera images. The yellow, orange and red curves in the line plots (Fig. 5C-G) represent the smoothed data of the accelerometer x, y, and z axes respectively, the grey curves represent the raw data for each axis. The blue curve shows the battery voltage, and the blue horizontal dashed line represent the 3.3 V threshold below which the battery is discharged and faulty behaviour may be expected.

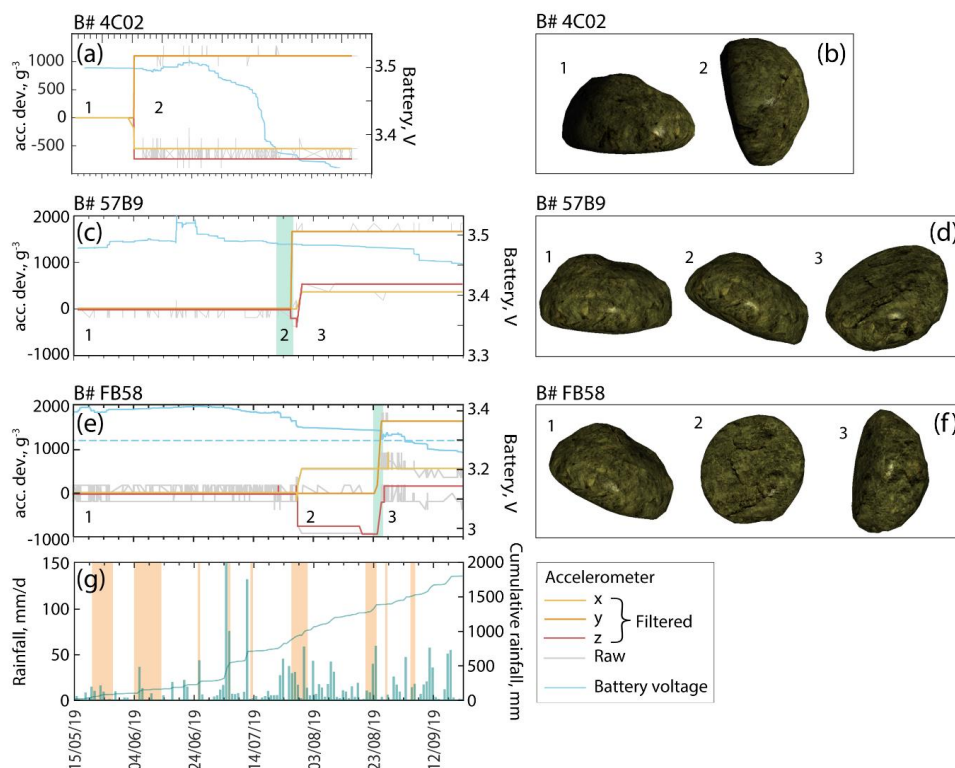


Fig. 6. Accelerometer data deviation from initial position for boulders in the debris flow channel and its banks through the monsoon season. Light green bars represent uncertainty in the movement timing due to lack of GPS acquisition (i.e. no time recorded) or offline gateway. A) Daily and cumulative rainfall data from GPM. Yellow bars represent days in which movements are observed in the channel and/or on its banks in the field camera images. B-C-D) Model boulder 3D visualisation to represent the change from the initial positions of the boulders and the positions acquired after the recorded movement. Numbers of positions are marked in the accelerometer graphs.

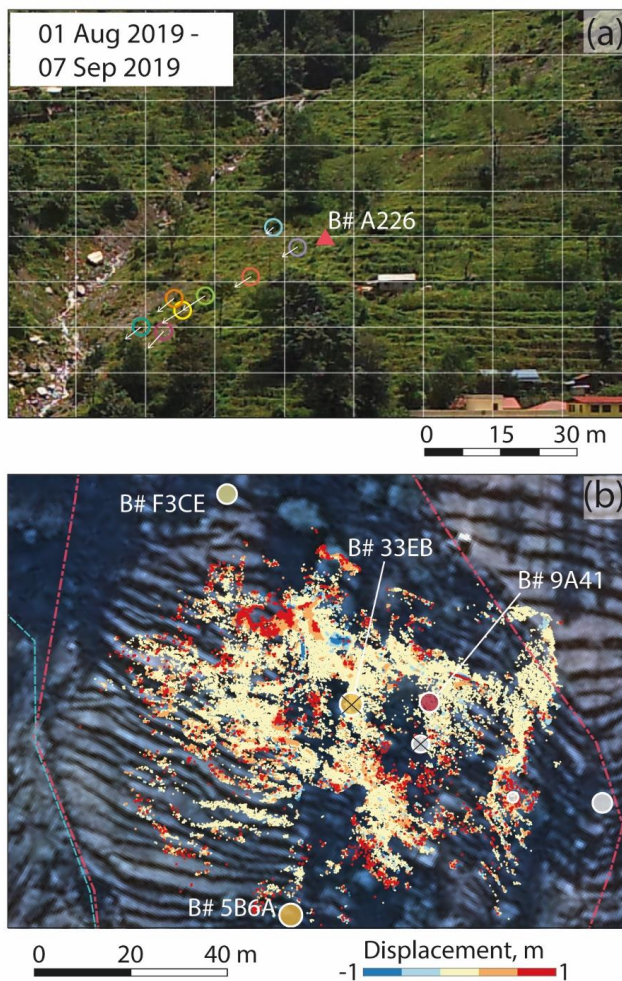


Fig. 7. Examples of movements in the landslide body between A and B. Coloured circles represent visually traceable pixels. Their movement is visible through the superposed grid. Approximate location of B# A226 is shown. C) Scan data for the upper part of the landslide area shows several zones of movement, where red represents accumulation and blue erosion. Black crosses over the boulders represent boulders that were not found after the monsoon season. Image: Pleiades (CEOS Landslides Pilot).

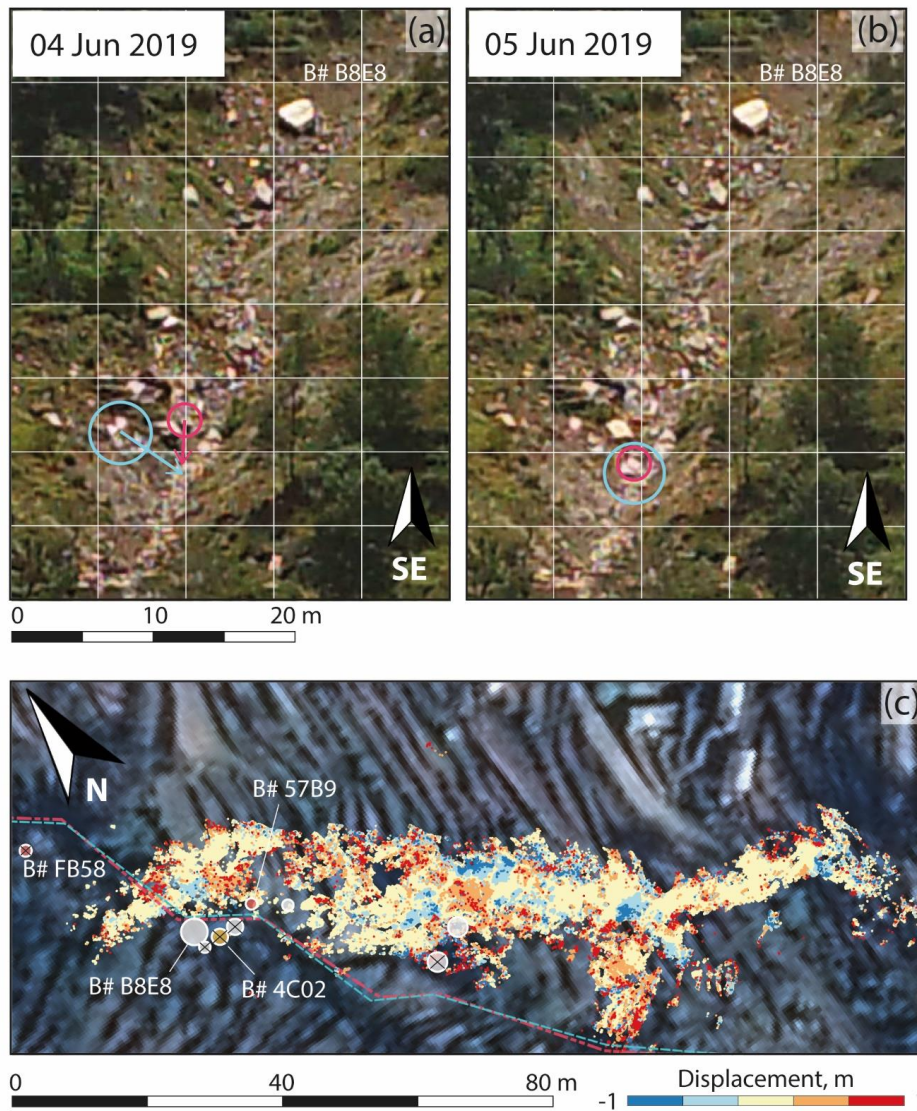


Fig. 8. Example of movements in the debris flow channel between A and B. Example of movements in the channel banks and in the channel between C and D. Coloured circles represent traceable pixels. Coloured boxes represent areas in which large changes are observed. E) Scan data for the channel showing several zones of movement, blue represent collapse of parts of the orographic right bank, red represents accumulation areas. Black crosses over the boulders represent boulders that were not found after the monsoon season. Image: Pleiades (CEOS Landslides Pilot).

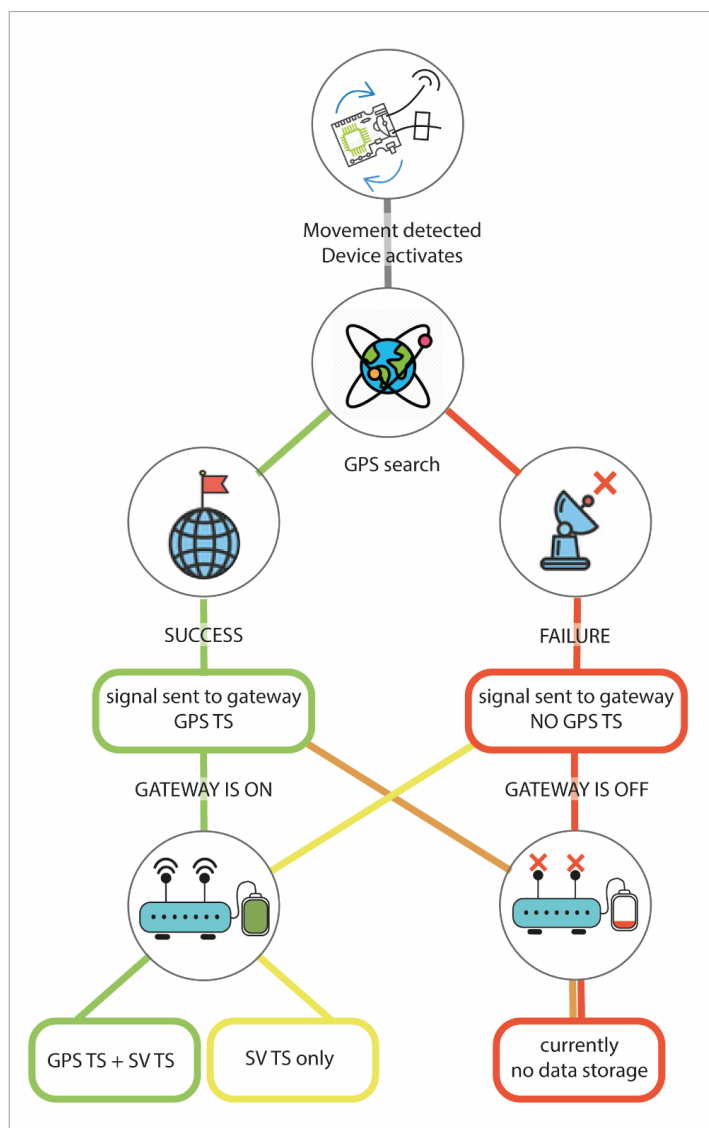
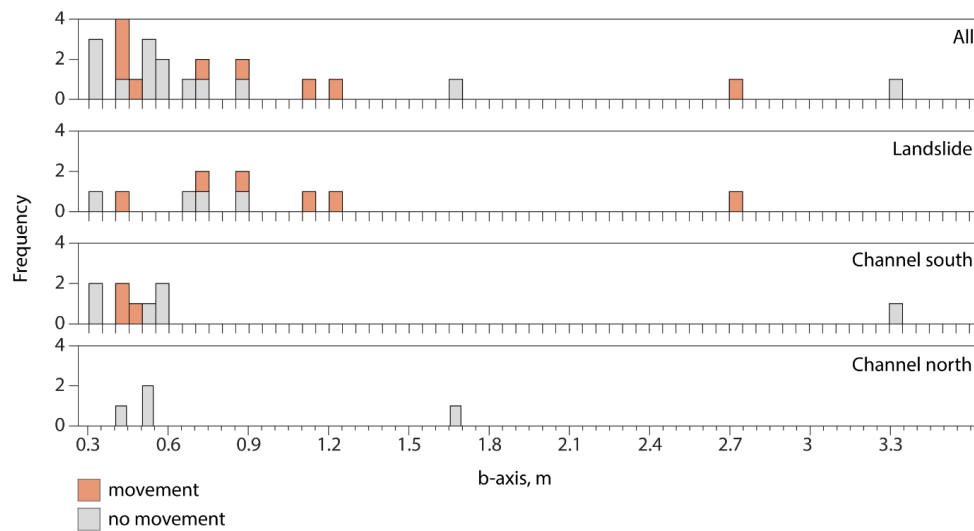
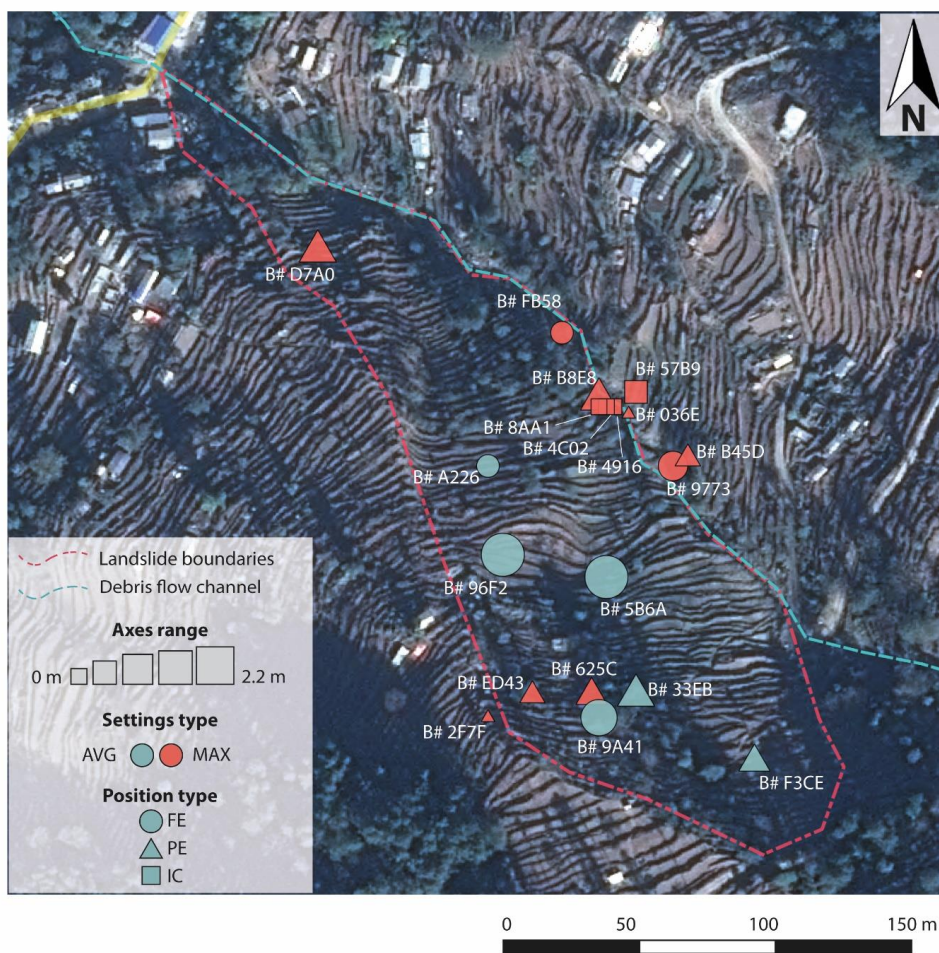


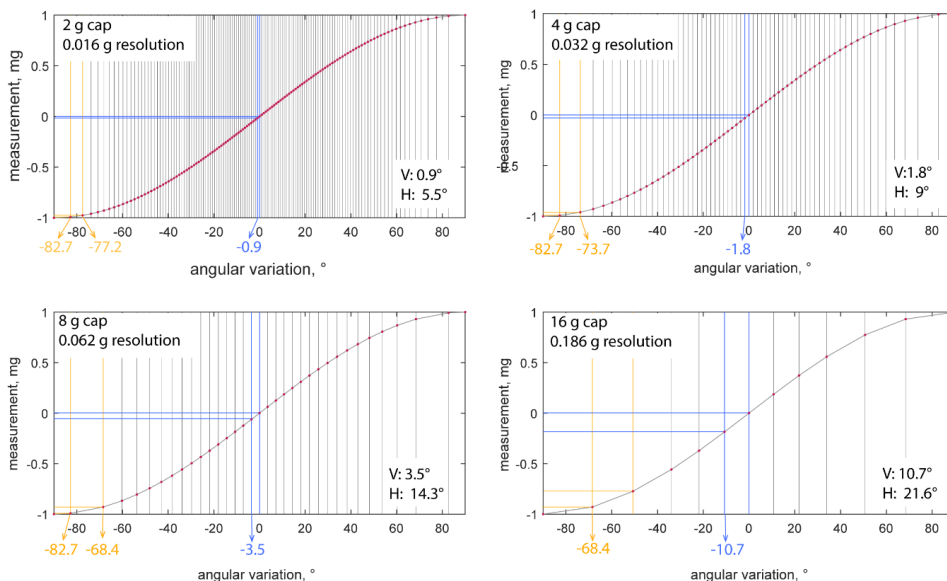
Fig. 9. Flowchart illustrating the presence of GPS timestamp (GPS TS) and server timestamp (SV TS) and the different scenario of GPS acquisition and data transmission.



A1. Histograms of boulders b-axis. Colours indicate boulders with movement (light red) or no movement (grey), whilst the panels, top to bottom represent all boulders, landslide boulders, and boulders in the south and north channels respectively. Boulders within the landslide show movements even when their sizes are large, whilst those in the southern channel had preferentially b-axis between 0.4 and 0.5 m.



A2. Zoom of two tagged sites. Sizes represent the range between the a-axis and the c-axis of the boulders (equal axes, range 0; most elongated boulders, range 2.2). Sizes are shown in legend for squared symbols but apply to all boulders. Colours represent setting types and symbols represent location type. Image: Pleiades (CEOS Landslides Pilot).



A3. Resolution and sensitivity of the accelerometer with scale capped at 2, 4, 8, and 16 g respectively. The vertical lines represent the angular variation corresponding to each step in the scale (mg). The graphs show that for increasing maximum detectable value, the resolution decreases significantly. Moreover, the sensitivity is higher when the axis is vertical than when the axis is horizontal, i.e. when the axis is near horizontal, a larger angular variation is required to make one step in the g scale. Thus, the angular threshold used to trigger a fix has to be higher than the maximum angular change needed to make a step in the g scale when the axis is near horizontal. This is shown as H in the text box in the plots.